Please, cite as: D'Alessandro, V., Montelpare, S., Ricci, R., "Detached–eddy simulations of the flow over a cylinder at Re = 3900 using OpenFOAM", Computers and Fluids, 2016, 136, pp. 152–169
doi: https://doi.org/10.1016/j.compfluid.2016.05.031

Detached–Eddy Simulations of the flow over a cylinder at Re = 3900 using OpenFOAM

Valerio D'Alessandro [a,*], Sergio Montelpare [b], Renato Ricci [a]

[a] *Dipartimento di Ingegneria Industriale e Scienze Matematiche*
Università Politecnica delle Marche
Via Brecce Bianche, 60100 Ancona (AN), Italy

[b] *Dipartimento di Ingegneria e Geologia*
Università degli Studi "G. D'Annunzio" di Chieti-Pescara
Viale Pindaro 42, 65127, Pescara (PE), Italy

Abstract

In this paper we present Detached–Eddy Simulations (DES) of the flow field past a cylinder at Reynolds number 3900 obtained by means of the open–source code OpenFOAM.

A first aim of the work was to implement a complex DES model based on the $\overline{v^2}$–f approach in order to take advantage of its good performance in the near-wall as well as in the LES region. The model was tested successfully against the selected benchmark case using a Dirichlet type wall boundary condition for the ϵ equation. The role of non–linear constitutive relations in unsolved term modelling was also investigated, but only for the standard Spalart–Allmaras DES approach. A second aim of this study was to validate the DES models available in the OpenFOAM official release.

Supercomputing facilities are essential for DES computations to be performed within an acceptable wall–clock time, so we also conducted a detailed code scalability assessment on latest-generation supercomputing equipment. These results are also extensively discussed in this paper.

Key words:
Detached–Eddy Simulation, OpenFOAM, Cylinder Flow, HPC.

1 Introduction

Nowadays it is well known that unsteady Reynolds–Averaged Navier–Stokes (RANS) models fail to predict proper flow physics in many cases involving large turbulent structures. On the other hand, Large-Eddy Simulations (LES) require a very fine grid in the near-wall region, and thus entail a high computational cost. The Detached-Eddy Simulation (DES) technique introduced by Spalart et al. [1], is a hybrid RANS/LES approach that operates like RANS in the near-wall regions and like LES in separated flow zones. DES is probably the most popular hybrid RANS/LES method because it is simple to apply to a wide range of existing RANS models. It is also particularly attractive because it produces good results in several conditions with fewer computational resources than standard LES. The original DES formulation is based on the Spalart-Allmaras (SA), [2], eddy-viscosity RANS model, for which LES behavior is achieved by modifying the length scale used in the turbulence model. It is worth mentioning that standard DES approaches raise some practical issues and have been harder to deal with than was initially expected by the CFD community. An extended review of these issues, *i.e.* Modeled–Stress Depletion (MSD), Grid–Induced Separation (GIS) and log–layer mismatch, can be found in [3]. GIS problems as a consequence of the MSD effect were solved by using a Delayed–Detached–Eddy Simulation (DDES) model, [4], and that

* Corresponding author.
Email addresses: v.dalessandro@univpm.it (Valerio D'Alessandro), s.montelpare@unich.it (Sergio Montelpare), ricci@univpm.it (Renato Ricci).

is why DDES can be considered the new standard version of DES. The improved Delayed–Detached–Eddy Simulation (IDDES) approach, [5], is more ambitious. It was developed, complete with new empirical functions, to overcome the log–layer mismatch as well as MSD. DES models have also since been introduced that are based on two–equation RANS. In particular, Travin et al. [6] developed a DES model based on the SST k–ω model, and other modifications were proposed in various papers too (for this specific model), that involved replacing the length scale in the transport equations for turbulence, [7, 8, 9].

It is only very recently that DES approaches based on the $\overline{v^2}$–f RANS model have appeared in the literature. A first advantage of this model by comparison with other RANS methods lies in its ability to accurately predict the near-wall effects without specific treatments or expedients. Jee and Shariff, [10], introduced a DES approach based on the k–ϵ–$\overline{v^2}$–f model; Mirzaei and Sohankar, [11], developed a k–ω–$\overline{v^2}$–f DES technique; and Ashton et al., [12], pursued a DES approach using the ϕ–f model. These models are very appealing for DES development purposes because they use a length scale based on flow properties, not on grid size like the SA model. In LES mode, the $\overline{v^2}$–f DES models also have a transport equation for the Sub–Grid Scales (SGS) kinetic energy that is less empirical than the SGS modified turbulent viscosity, $\tilde{\nu}$, used in the standard SA–DES. The main drawback of these models lies in that they use four additional equations for turbulence modeling, while other DES techniques are less costly from this point of view.

The sphere and the circular cylinder are obvious test cases for an approach with claims over separated flows [13, 14]. In this paper, we focus our efforts on the flow over the circular cylinder in the lower sub–critical range at Re = 3900. A first set of experimental measurements was conducted on this flow field by

Lourenco and Shih [15] using PIV equipment. More recently, Parnaudeau et al. [16] performed numerical simulations (LES) and experiments with the PIV and HWA methods. Their PIV data are not consistent with those obtained by Lourenco and Shih in the very near wake, but both data sets are consistent with the HWA data obtained by Ong and Wallace, [17], far away from the near wake. That is why some authors have claimed there is a flow bifurcation in the very near wake region. To be more precise, a first flow state is characterized by the presence of a U–shaped profile of the stream-wise velocity, while a second state reveals the presence of a V–shaped profile. Both states have been found in a large number of LES and Direct Numerical Simulations (DNS). Moin, [18], recently confirmed that the U–shaped state is correct, however, and that the V–shaped profile occurs in experiments due to vibrations. It is important to note that the computation of solutions with U–shaped profiles is no trivial task. This specific flow problem has consequently become a popular case for testing numerical modelling and most of the publications have been concerned with LES, [16, 19, 20, 21, 22, 23, 24, 25, 26, 27, 28, 29, 30, 31, 32]. A DNS computation was conducted in Ma et al. [33], while Wissink and Rodi, [34], performed a series of DNS tests for a flow over a circular cylinder at Re = 3300. On the other hand, DES computations of this flow field are quite limited. Xu et al, [14], applied standard SA–DES, while Jee and Shariff, [10], more recently performed SA–DDES and DES based on their own $\overline{v^2}$–f approach, obtaining very good results. Zhao et al., [35], performed a series of DES simulations using high–order schemes and standard SA–DES, while Li et al., [36], used the same approach to solve the flow equations with an immersed boundary method.

In this paper, we present a suite of DES computations of the flow over the circular cylinder at Re = 3900 using OpenFOAM code, [37]. This is an open–

source code based on an unstructured finite volume method (FVM), released under the GNU Public License (GPL). In recent years it has attracted a great deal of interest from both academic institutions and industry because it provides accurate solutions and also allows for customization.

Here we describe an implementation and an assessment of recent DES techniques in OpenFOAM. We also thoroughly investigate and validate the standard DES models available in official releases. The parallel scalability of the code adopted is also carefully analyzed on latest-generation supercomputing facilities.

This paper is organized as follows. Sec. 2 presents the governing equations of the DES approaches considered here. Sec. 3 briefly describes the discretization technique and OpenFOAM parallel scalability. Sec. 4 is devoted to the numerical results, and Sec. 5 contains the conclusions.

2 Governing equations

This section describes the flow models used in this paper. Several variants of the SA–DES approach and a DES technique based on the $\overline{v^2}$–f model were tested.

The SA–DES/IDDES approaches were used with the OpenFOAM native implementation, while the $\overline{v^2}$–f DES approach was implemented here within the OpenFOAM code for the first time. We also report on an investigation into the role of non–linear quadratic constitutive relations for turbulent unsolved terms (relating only to the Spalart–Allmarar DES model).

The original DES model was introduced by Spalart et al., [1], and it replaces the minimum wall distance d in the SA–RANS model with a modified length scale $\tilde{d}$:

$$\tilde{d} = \min\left(d, C_{DES}\Delta\right), \quad \Delta = \max\left(\Delta x, \Delta y, \Delta z\right), \tag{1}$$

where Δx, Δy and Δz are the grid sizes and C_{DES} is a constant. In the boundary layer, the normal wall distance d is actually much smaller than the wall parallel grid spacing. The modified normal wall distance consequently acts as a length scale, $\tilde{d} = d$, and the SA–RANS model is retained within the boundary layer. Outside the boundary layer, on the other hand, the normal wall distance is larger than the grid spacing, so the modified length scale becomes $\tilde{d} = C_{DES}\Delta$. Being dependent on the grid size, this length scale enables the DES model to work like LES in separated flow regions, which are typically located away from the walls.

The complete set of the incompressible SA–DES Partial Differential Equation (PDE) system can be written as:

$$\begin{aligned}
&\boldsymbol{\nabla}\cdot\mathbf{u} = 0,\\
&\frac{\partial \mathbf{u}}{\partial t} + \boldsymbol{\nabla}\cdot(\mathbf{u}\otimes\mathbf{u}) = -\frac{1}{\rho}\boldsymbol{\nabla}p + \boldsymbol{\nabla}\cdot(2\nu\mathbf{D}) + \boldsymbol{\nabla}\cdot\mathbf{B},\\
&\frac{\partial \tilde{\nu}}{\partial t} + \boldsymbol{\nabla}\cdot(\mathbf{u}\tilde{\nu}) = c_{b1}\tilde{S}\tilde{\nu} + \frac{c_{b2}}{\sigma}\boldsymbol{\nabla}\tilde{\nu}\cdot\boldsymbol{\nabla}\tilde{\nu} + \frac{1}{\sigma}\boldsymbol{\nabla}\cdot\left(\left(\nu+\tilde{\nu}\right)\boldsymbol{\nabla}\tilde{\nu}\right) - c_{w1}f_w\left(\frac{\tilde{\nu}}{\tilde{d}}\right)^2.
\end{aligned} \tag{2}$$

The unsolved term, tensor $\mathbf{B}$ in eq. 2, is modelled in this work as:

$$\mathbf{B} = \mathbf{R} - c_{r1}\left(\mathbf{Q}\cdot\mathbf{R} - \mathbf{R}\cdot\mathbf{Q}\right), \tag{3}$$

where $\mathbf{R}$ is the linear part of $\mathbf{B}$, which is expressed in terms of the classic Boussinesq approximation:

$$\mathbf{R} = -\frac{2}{3}k\mathbf{I} + 2\nu_t\mathbf{D}, \tag{4}$$

where $\nu_t = f_{v1}\tilde{\nu}$ and $\mathbf{D} = 0.5\left(\boldsymbol{\nabla}\mathbf{u} + \boldsymbol{\nabla}\mathbf{u}^T\right)$. The non–linear term appearing in eq. 3 was introduced by Spalart in [38] for RANS equations coupled with the SA model. This quadratic constitutive relation uses only one of the many possible combinations of strain rate and rotation tensor, and it is related to the proposal advanced by Wilcox and Rubesin, [39]. The constant c_{r1} was obtained by Spalart himself in [1] for simple boundary layer flows with the constraint $\overline{u'u'} > \overline{w'w'} > \overline{v'v'}$. The value obtained for c_{r1} is 0.3. The normalized rotation tensor $\mathbf{Q}$ in eq. 3 is defined as:

$$\mathbf{Q} = 2\boldsymbol{\Omega}/\sqrt{\boldsymbol{\nabla}\mathbf{u} : \boldsymbol{\nabla}\mathbf{u}}, \quad \boldsymbol{\Omega} = \frac{1}{2}\left(\boldsymbol{\nabla}\mathbf{u} - \boldsymbol{\nabla}\mathbf{u}^T\right).$$

The following closure functions are now introduced to complete the definition of the PDE system reported in eq. 2:

$$\begin{aligned}
f_{v1} &= \frac{\chi^3}{(\chi^3 + c_{v1}^3)}, & f_{v2} &= 1 - \frac{\chi}{(1 + \chi f_{v1})}, \\
g &= r + c_{w2}\left(r^6 - r\right), & f_w &= g\left[\frac{1 + c_{w3}^6}{g^6 + c_{w3}^6}\right]^{\frac{1}{6}}, \\
r &= \frac{\tilde{\nu}}{\tilde{S}k^2d^2}, & \tilde{S} &= S + \frac{\tilde{\nu}}{k^2d^2}f_{v2},
\end{aligned} \tag{5}$$

where $S = \sqrt{2\boldsymbol{\Omega} : \boldsymbol{\Omega}}$ and $\chi = \tilde{\nu}/\nu$. The closure parameters are those of the standard model:

$$\begin{aligned} c_{b1} &= 0.1355, \quad c_{b2} = 0.622, \quad c_{v1} = 7.1, \\ \sigma &= 2/3, \quad c_{w1} = \frac{c_{b1}}{k^2} + \frac{(1 + c_{b2})}{\sigma}, \\ c_{w2} &= 0.3, \quad c_{w3} = 2, \quad k = 0.41. \end{aligned} \tag{6}$$

It is important to note that few papers in literature have chosen, as we did, to adopt a non–Boussinesq constitutive relation for tensor $\mathbf{B}$. A seminal work in the LES environment was conducted by Liu et al., [40], while Gopalan and Jaiman, [41], very recently developed two different non–linear hybrid RANS–LES approaches. These works essentially showed that non–linear methods might contribute a small, but robust improvement to a basic technique.
From now on, we refer to DES based on the SA model with a non–linear constitutive relation as Non–Linear Detached–Eddy Simulation (NLDES), and to the standard technique using the common Boussinesq approximation ($c_{r1} = 0$) as SA–DES.

2.2 The SA–IDDES model

The goal of the SA–IDDES model is to combine the advantages of the wall modeled LES (WMLES) with DDES capabilities. The IDDES approach avoids the issue of mismatch between the modelled log–layer and the solved log–layer, which has typically plagued the use of either DES or DDES for wall modelling in LES. IDDES incorporates the different approaches involved in the following manner:

$$l_{IDDES} = \tilde{f}_d \left(1 + f_e\right) l_{RANS} + \left(1 - \tilde{f}_d\right) l_{LES} \tag{7}$$

where l_{LES} is defined as $C_{DES}\Delta$. The grid scale Δ is defined as $\min\left[C_w\Delta_{max}, C_w d, \Delta_{min}\right]$, where C_w is a constant and d is the distance from the nearest wall; Δ_{min} is taken as $\min\left(\Delta x, \Delta y, \Delta z\right)$ and Δ_{max} equals $\max\left(\Delta x, \Delta y, \Delta z\right)$. The $\tilde{f}_d$ function is defined as $\max\left(1 - f_{dt}, f_B\right)$ which is determined by both the geometry and the flow.

When $f_e = 0$, l_{IDDES} in eq. 7 can be written as:

$$l_{IDDES} = \tilde{f}_d l_{RANS} + \left(1 - \tilde{f}_d\right) l_{LES} \tag{8}$$

and IDDES is converted into DDES. Conversely, when $f_e > 0$ and $\tilde{f}_d = f_B$, l_{IDDES} is written as:

$$l_{IDDES} = f_B\left(1 + f_e\right) l_{RANS} + \left(1 - f_B\right) l_{LES} \tag{9}$$

and IDDES behaves in WMLES mode in the wall region. The detailed formulations of the functions not described here for the sake of brevity can be found in the original reference, [5]. Note that l_{IDDES} is the length scale required from the $\tilde{\nu}$ transport equation in the DES framework.

2.3 The $\overline{v^2}$–f DES model

The DES approach based on the v^2–f model tested here is drawn from the version of the v^2–f RANS model proposed by Lien et al., [42]. This model has a transport equation for k, ϵ and $\overline{v^2}$ together with an elliptic relaxation equation for a function f containing the time and length scales. The choice between RANS and LES models is made on the grounds of the standard DES criterion, introduced by Spalart et al. in [1], relating to the flow scales.

The flow model equations read as follows:

$$\begin{aligned}
&\frac{\partial k}{\partial t} + \boldsymbol{\nabla}\cdot(\mathbf{u}k) = \mathbb{P} - \epsilon_{DES} + \boldsymbol{\nabla}\cdot\left[(\nu+\nu_t)\,\boldsymbol{\nabla}k\right],\\
&\frac{\partial \epsilon}{\partial t} + \boldsymbol{\nabla}\cdot(\mathbf{u}\epsilon) = \frac{c_{\epsilon 1}\mathbb{P} - c_{\epsilon 2}\epsilon}{T_{DES}} - \epsilon_{DES} + \boldsymbol{\nabla}\cdot\left[\left(\nu + \frac{\nu_t}{\sigma_\epsilon}\right)\boldsymbol{\nabla}\epsilon\right],\\
&\frac{\partial \overline{v^2}}{\partial t} + \boldsymbol{\nabla}\cdot\left(\mathbf{u}\overline{v^2}\right) = kf_{DES} - 6\frac{\overline{v^2}}{k}\epsilon_{DES} + \boldsymbol{\nabla}\cdot\left[(\nu+\nu_t)\,\boldsymbol{\nabla}\overline{v^2}\right],\\
&c_L^2 L_{DES}^2\boldsymbol{\nabla}^2 f - f = \frac{1}{T_{DES}}\left[(c_1-6)\,\frac{\overline{v^2}}{k} - \frac{2}{3}(c_1-1)\right] - c_2\frac{\mathbb{P}}{k}
\end{aligned} \tag{10}$$

where the eddy–viscosity is considered as: $\nu_t = c_\mu \overline{v^2} T_{DES}$. The switch from the RANS to the LES mode is based on the comparison of the length scale $k^{3/2}/\epsilon$ and the grid size, Δ. To be specific, if $k^{3/2}/\epsilon < C_{DES}\Delta$, the model works in RANS mode with the following conditions:

$$L_{DES} = L_{RANS}, \quad T_{DES} = T_{RANS}, \quad \epsilon_{DES} = \epsilon, \tag{11}$$

where:

$$\begin{aligned}
T_{RANS} &= \min\left[\max\left[\frac{k}{\epsilon}, c_T\left(\frac{\nu}{\epsilon}\right)^{1/2}\right], \frac{0.6k}{\sqrt{6}c_\mu\overline{v^2}\,|\mathbf{D}|}\right],\\
L_{RANS} &= \max\left[\min\left[\frac{k^{3/2}}{\epsilon}, \frac{k^{3/2}}{\sqrt{6}c_\mu\overline{v^2}\,|\mathbf{D}|}\right], c_\eta\left(\frac{\nu^3}{\epsilon}\right)^{1/4}\right];
\end{aligned} \tag{12}$$

if not, the model operates in LES mode as follows:

$$L_{DES} = C_{DES}\Delta, \quad T_{DES} = C_{DES}\Delta/\sqrt{k}, \quad \epsilon_{DES} = k^{3/2}/(C_{DES}\Delta). \tag{13}$$

The production term in the transport equation for the turbulent kinetic energy k is modelled as $\mathbb{P} = 2\nu_t\,|\mathbf{D}|^2$, whereas the production term in the equation for $\overline{v^2}$ is expressed with the following equation:

$$kf_{DES} = \min\left(kf, 5\frac{\overline{v^2}}{k}\epsilon_{DES} + \frac{2}{3}\mathbb{P}\right). \tag{14}$$

The model constants are the same as those proposed by Jee and Shariff in [10]:

$$
\begin{aligned}
&c_\mu = 0.22, \quad \sigma_\epsilon = 1.3, \quad c_{\epsilon 1} = 1.4\left(1 + 0.045\sqrt{k/\overline{v^2}}\right), \\
&c_{\epsilon 2} = 1.9, \quad c_1 = 1.4, \quad c_2 = 0.3, \\
&c_T = 6, \quad c_L = 0.23, \quad c_\eta = 70, \quad C_{DES} = 0.8.
\end{aligned}
\tag{15}
$$

As for the boundary conditions, we adopted the same set of conditions as those proposed in [10]. The wall condition for the ϵ equation was treated differently, however. In this work we did not adopt the condition $\epsilon_w = \nu \partial_n^2 k|_w$ used in [10]; we implemented the formulation proposed by Chien, [43], for RANS equations instead. This type of condition is obtained by introducing, close to the wall, Taylor expansions for average velocity components and their fluctuations. Starting from the definition of ϵ, the condition at the wall reads:

$$
\epsilon_w = \nu \frac{2k}{y^2}. \tag{16}
$$

It is worth noting that Chien's wall boundary condition for ϵ is of the Dirichlet type, and it does not require an assessment of the second derivative for k, so it is easy to implement with no loss of second-order spatial accuracy.

3 Numerical solution

All computations in this work were performed using OpenFOAM v.2.3.0. In particular, we have used `pisoFoam`, which is the transient solver for incompressible flows available in official OpenFOAM releases. `pisoFoam` uses the well-established PISO algorithm, [44], for pressure–velocity decoupling and,

like the other standard solvers, it is based on a colocated FVM approach; the Rhie–Chow correction is used to remove oscillations in the solutions, [45].
All diffusive terms and pressure gradients were approximated with a second–order accuracy while a second–order implicit Euler method (BDF–2, [46]) was used for time integration.
For all the SA–DES/IDDES computations the convective terms were discretized using a limited central difference scheme, based on a limiter introduced by Sweby, [47], for the turbulence equation; a second-order central scheme was used for the momentum equation. Such a numerical setup revealed numerical stability problems for the $\overline{v^2}$–f DES computations in our preliminary test, so the high–resolution NVD Gamma scheme, [48], was chosen for the convective terms, while retaining the same configuration for the diffusive contributions.

3.1 OpenFOAM parallel performance

For each conservation equation, the linear system deriving from the implicit treatment of the unknown variables can be solved using different approaches available in OpenFOAM. It is common knowledge, however, that the structure of linear algebra solvers, matrix preconditioners and smoothers strongly influences the scaling behavior and overall computational efficiency of a CFD code. Ascertaining the parallel behavior of OpenFOAM on latest-generation supercomputers thus becomes essential in order to exploit these resources correctly. In our specific case, all the simulations were conducted on the GALILEO supercomputing facility at CINECA (a Tier–1 system forming part of the PRACE initiative, [49]), which is an IBM NeXtScale cluster consisting of 516 compute nodes with 2 octa–core Intel Haswell processors (E5–2630) with 2.40

GHz and 128 GB of RAM each. The system is also accelerated with 2 Intel Phi 7120p accelerators per node on 384 nodes and 2 NVIDIA K80 cards per node on 40 nodes.

To investigate the parallel scalability of the OpenFOAM code and run the DES computations as efficiently as possible, we considered a widely–used benchmark, i.e. the lid–driven cavity problem of a laminar, incompressible flow in a 3D cubic domain. All the boundaries were treated as walls except for the top, which was a moving wall. The strong scaling tests were conducted on a suite of four uniformly-spaced grids with a number of cells n_c amounting to: 10^6, $2 \cdot 10^6$, $3 \cdot 10^6$ and $4 \cdot 10^6$. We also fixed Re = 10 and $\Delta t = 10^{-4} H/u_w$ with a top wall velocity u_w and a cavity side size H; as linear solvers we used a preconditioned conjugate gradient method (PCG) with a diagonal incomplete Cholesky preconditioner for the pressure; an iterative solver based on the Gauss–Siedel method as a smoother was used for the velocity. The convergence tolerances were set to 10^{-6} for the pressure and 10^{-5} for the velocity. The scalability tests for this benchmark were conducted using the`icoFoam` solver and adopting two PISO correctors. The tests were conducted without any I/O for 40 time–steps, as in Culpo, [50], in order to cancel the starting overhead. Fig. 1 shows a first set of wall–clock time measurements. The effect of computational mesh size is clearly trivial, see Fig. 1(a), while the impact of both the compilers and of MPI library implementation is shown in Fig. 1(b). In this study, we also built OpenFOAM using Intel 15.0.2 and GNU 4.9.2 compilers, while IntelMPI v5.0.2 and OpenMPI v1.8.4 (built with both Intel and GNU compilers) were considered for message passing. Fig. 1(b) shows that using the different combinations of compilers and MPI implementations affords no evident gain in performance. This behavior was noted by Culpo too, [50], on the previous generation of Tier–0 and Tier–1 facilities, and it probably relates

to the storage format used for sparse matrix representation, which prevents an efficient use of SSE vectorization.

Fig. 2 shows the effect of the grid–size on OpenFOAM scalability in terms

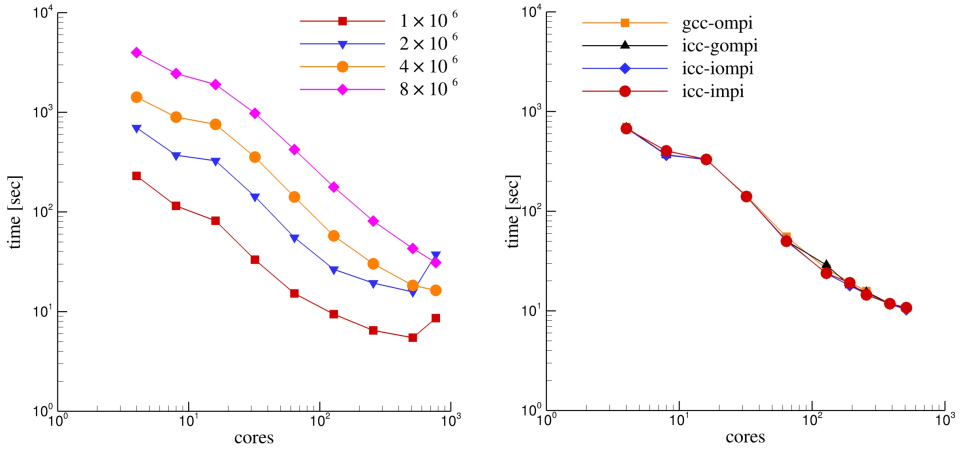

(a) Grid–size effect

(b) Compiler and MPI effect. $n_c = 2 \cdot 10^6$

Figure 1. Wall–clock time measurement.

of speedup and parallel efficiency. From here on, OpenFOAM computational performance is examined using GNU compilers and OpenMPI. It is worth noting that the intra–node scalability (up to 16 MPI tasks) is not optimal due to the bandwidth dedicated to memory as the number of tasks increases. The inter–node scalability shows an opposite trend up until the latency due to node communications becomes predominant. It is also worth noting that smaller grids have a better parallel performance with a reduced number of cores, see Fig. 2(b), while grids with more cells perform better using a large number of CPU–cores. In particular, we noted that OpenFOAM on GALILEO has a parallel efficiency of about 62% with 768 CPU–cores using the grid where $n_c = 8 \cdot 10^6$. This result shows that PISO-based solvers (such as `icoFoam`) can achieve a good parallel performance (about 10^4 cells for each core) on modern Tier–1 systems.

The influence of the linear solvers on parallel performance was also investi-

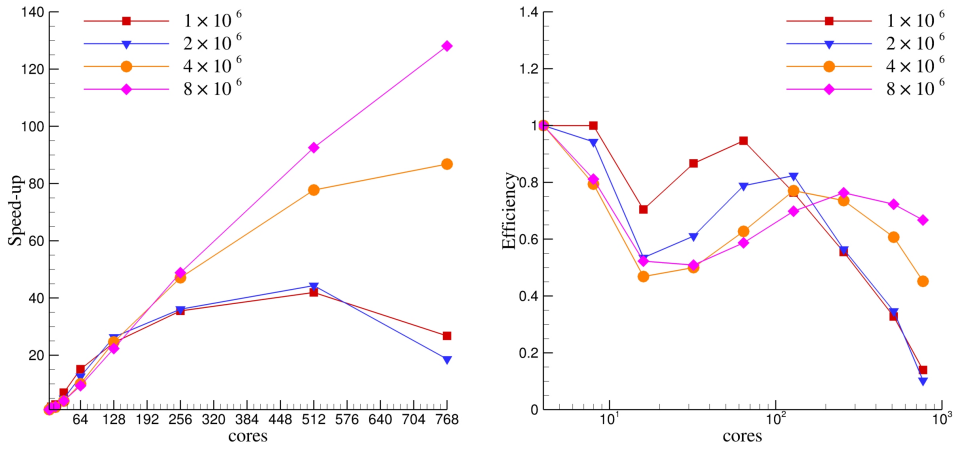

(a) Speed–up (b) Efficiency

Figure 2. Grid–size effect.

gated because, as Jasak has already pointed out, [51], the scalability and performance issues for OpenFOAM are both related to the sparse linear algebra core libraries. We studied these scalability properties using two different linear solvers for the pressure equation because its solution has a strong impact on the code's parallel performance. We considered a Geometric Agglomerated algebraic Multi–Grid (GAMG) solver and a Preconditioned Conjugate–Gradient (PCG) method (see for more details [52]). As already mentioned in several research papers, the GAMG linear solver is globally faster than the PCG one. This was confirmed by our tests too, as shown in Fig. 3, but this behavior only applies to computations without a very large number of CPU–cores. We also investigated the effect of the number of cells on the lowest level of the multi–grid approach implemented in GAMG. As expected, the increase in the number of cells on the lowest level negatively affects the solver's overall scalability properties, as shown in Fig. 4 and Fig. 5. It is worth noting, however, that the PCG solver has better scalability properties than the GAMG solver. This feature relates to the communication overload produced by GAMG on its coarsest level.

Our scalability study enabled us to gain a thorough understanding of the

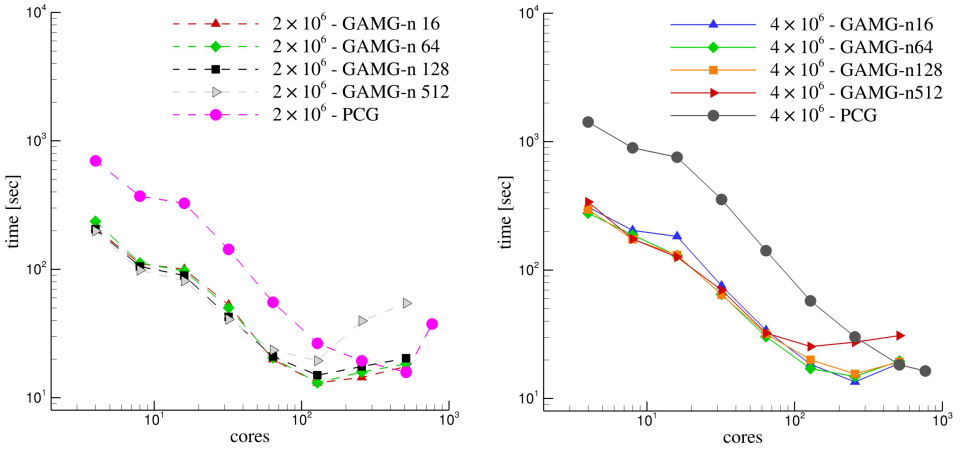

(a) $n_c = 2 \cdot 10^6$ (b) $n_c = 4 \cdot 10^6$

Figure 3. Linear solver effect. Wall–clock time.

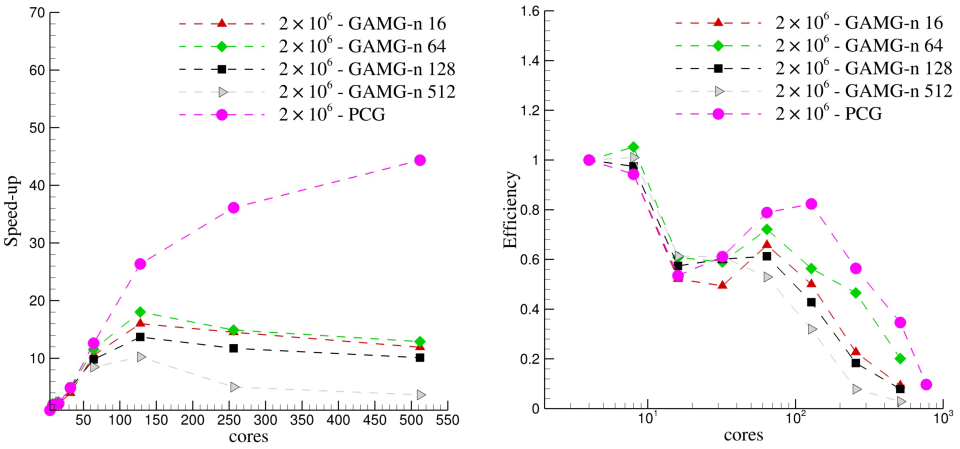

(a) Speed–up (b) Efficiency

Figure 4. Linear solver effect. Grid with $n_c = 2 \cdot 10^6$.

parallel behavior of the OpenFOAM linear solver used on latest-generation supercomputers. In the light of these results, we went on to perform our DES computations using a PCG solver for the pressure and OpenFOAM v2.3, built using GNU compilers and OpenMPI, for message passing. This linear solver configuration enabled us to exploit the GALILEO facility as efficiently as possible.

In the DES cases, we used a preconditioned bi–conjugate gradient method

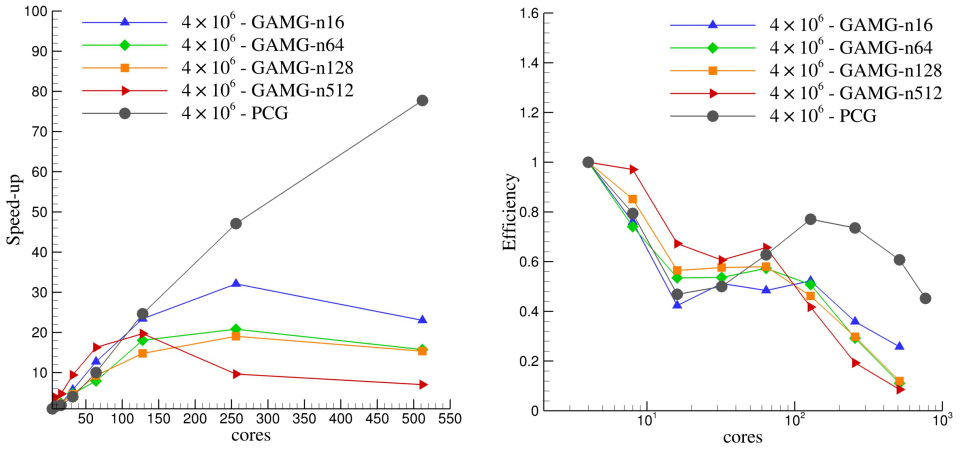

(a) Speed–up (b) Efficiency

Figure 5. Linear solver effect. Grid with $n_c = 4 \cdot 10^6$.

(PBiCG) with a diagonal incomplete–LU (asymmetric) preconditioner for the velocity and turbulence equations. For the pressure, on the other hand, we used a preconditioned conjugate gradient method (PCG) with a diagonal incomplete Cholesky preconditioner. The linear system for pressure was solved using a local accuracy of 10^{-6}, whereas the other systems were considered as having converged when the residuals reached 10^{-9}. For the turbulent variables we used the same approach as for the velocity, except for the elliptic relaxation function f, for which we used the same techniques as for the pressure, but the numerical solution was considered as having converged when the residuals reached 10^{-9}.

3.2 Computational domain

We built five different structured computational grids, the mean parameters of which are listed in Table 1. The finest grid, named G1, has $n_c = 3955200$ cells with a spanwise length L_z of πD discretized by 48 computational cells as in several other publications, [16, 20, 26, 27, 53, 54]. The estimation adopted

for the spanwise domain size and resolution was drawn from Kravchenko and Moin, [23], assessing the sizes of the streamwise vortex structures a priori. Previous authors have also shown that 48 cells suffice to capture the vortical structures developing behind the cylinder.

The G1 grid was created by uniformly extruding the longitudinal plane, shown in Fig. 6, which has a number of cells $n_{c,x,y}$ amounting to 82400. The G2 grid consists of 494400 cells and it was obtained by halving the G1 grid cells in all the x–y–z directions. The G3 grid was obtained starting from the same longitudinal plane discretization conceived for G1 grid, and applying a coarser discretization in the span–wise direction, using only 8 cells for a length of πD. The G4 and G5 grids were built adopting $L_z = 0.5D$ in order to examine the effect of the span–wise length of the domain. In both cases, we set $n_{c,x,y} = 82400$, as in G1 and G3. We used 8 cells for the G5 grid, so the spanwise resolution Δz was very similar to that of our finest grid (G1). For the G4 grid, we refined N_z up to 25 computational cells, obtaining $2.06 \cdot 10^6$ cells.

It should be noted that a distance of 10 D between the cylinder surface and the inflow boundary was used for all the grids; in the wake region the domain develops for 40 D behind the cylinder's surface. The distance between the upper and lower sides of the computational domain is 20 D, while the height of the cells next to the walls was set to: $\Delta r/D = 2 \cdot 10^{-4}$ for all the grids except G3, for which this value was doubled.

The computations involving the largest number of grid cells were completed on the GALILEO supercomputing facility at CINECA using 384 CPU–cores for the simulations relating to the G1 grid and 192 CPU–cores for the G4 grid. Note that the number of cores was chosen consistently with the scalability tests presented in Sec. 3.1; this choice stems from evidence of `icoFoam`

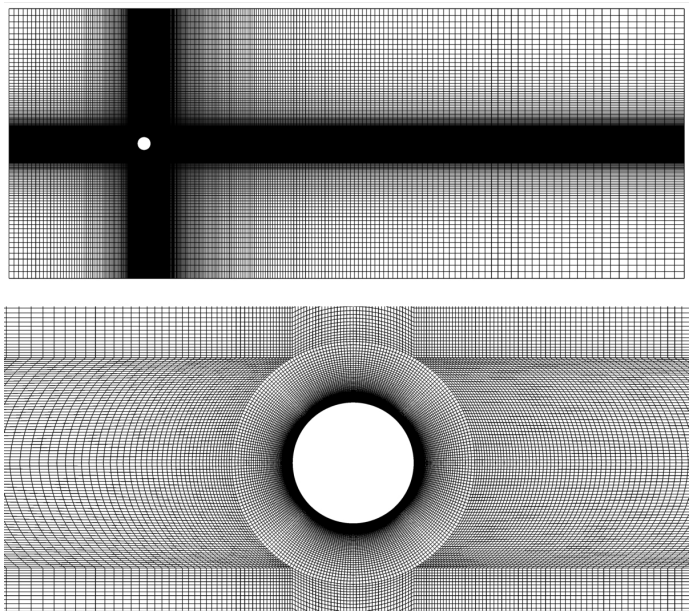

Figure 6. Representation of the computational grid.

Table 1
Computational grids parameters

	n_c	L_z	N_z	$n_{c_{x,y}}$	Δz
G1	3955200	πD	48	82400	$6.54 \cdot 10^{-2}$
G2	494400	πD	24	20600	$1.308 \cdot 10^{-1}$
G3	659200	πD	8	82400	$3.92 \cdot 10^{-1}$
G4	$2.06 \cdot 10^6$	$0.5D$	25	82400	$2 \cdot 10^{-2}$
G5	659200	$0.5D$	8	82400	$6.25 \cdot 10^{-2}$

and `pisoFoam` sharing the same numerical technology. The solutions on the coarser grids were obtained on a small Linux Cluster with 6 AMD Opteron-based nodes for a total of 96 CPU cores operating at 2.6 GHz.

4 Results

This section illustrates our numerical solutions for the flow field over a circular cylinder in the sub-critical regime at $\mathrm{Re} = 3900$.

For this case the flow is laminar in the boundary layer, even in the vicinity of the obstacle, and it becomes turbulent only after separation. There is also evidence of Kelvin–Helmoltz instabilities before the turbulent region. The proposed benchmark enables us to test the DES models considered as LES drawing a rigorous comparison with previously published studies. It is worth noting that, the flow being turbulent only after separation, any DES model can be expected to provide accurate LES results. It is important to emphasize that DES models have been developed specifically to work in RANS mode in the near–wall region; they have been designed for fully turbulent flows and calibrated with turbulence data. For this flow problem, we use a RANS model to handle a fully–laminar boundary layer. The flow features consequently reveal a critical issue related to our flow models. Most transport equation models converge towards laminar solution at low Reynolds numbers anyway. Several RANS models are also able to emulate a laminar–turbulent transition although the rigorous mathematical origin for this phenomenon is still not known, [55]. Roughly speaking, it could be said that the behavior of a specific RANS model in a laminar region is not strictly predictable. The results obtained are consequently used to discuss the ability of a specific model to describe a laminar layer, providing some indications concerning the turbulent viscosity in the boundary layer.

The description of the boundary conditions for the turbulence model equations can be found in Table 2. No wall functions were used and the flow periodicity was assumed to be in the span–wise direction; the inviscid wall condition was employed for the upper and lower sides of the domain.

Finally, for the purpose of a comparison with the literature, turbulence statistics were sampled over about 190 shedding periods, corresponding to a time interval of $T = 900D/u_\infty$ and a time–step size $\Delta t = 10^{-3}D/u_\infty$.

Table 2
Turbulent variable boundary conditions

	k	$\overline{v^2}$	ϵ	f	$\tilde{\nu}$
Initial Conditions	$10^{-3}u_\infty^2$	$2/3 \cdot 10^{-3}u_\infty^2$	$10^{-3}u_\infty^3/D$	0	3ν
Wall boundary	0	0	$2\nu k/y^2$	0	0
Inlet boundary	0	0	$\partial_n \epsilon = 0$	$\partial_n f = 0$	3ν
Outlet boundary	$\partial_n k = 0$	$\partial_n \overline{v^2} = 0$	$\partial_n \epsilon = 0$	$\partial_n f = 0$	$\partial_n \tilde{\nu} = 0$

4.1 Flow statistics

4.1.1 Grid study

This subsection concerns an extensive grid effect study for the different DES approaches considered in this paper. This topic is of interest because the grid resolution is particularly relevant to other turbulence simulation techniques, such as DNS and LES, as already noted in [23, 56].
For this purpose, the flow statistics emerging from our simulations with the G1 and G2 grids, combined with the following experimental data from the literature

(i) PIV data in Lourenco and Shih, [15],
(ii) PIV data in Parnaudeau et al., [16],
(iii) HWA data in Ong and Wallace, [17],

are shown in Figs. 7–10. Note that the G1 and G2 grids are nested and the ratio between their number of cells, n_c, is exactly 8.
Fig. 7 shows the mean streamwise velocity in the wake centerline, which is zero at the base of the cylinder (no–slip condition), then reaches a negative minimum value in the recirculation zones, and converges asymptotically toward

the free–stream velocity. From this plot we can also obtain the mean streamwise length of the recirculation region, $\langle L_r \rangle / D$. Note that, by definition, $\langle L_r \rangle$ corresponds to the distance between the cylinder surface and the sign change of the mean streamwise velocity along the centerline. It is therefore easy to use Fig. 7 to estimate $\langle L_r \rangle / D$. The mean streamwise and transverse velocity profiles in the cylinder's wake are also shown in Fig. 8 and in Fig. 9 respectively. Clearly, conflicting results for the very near wake ($x/D \leq 2.02$) emerge from the different experimental data considered here. In particular, Lourenco and Shih found a V–shaped streamwise velocity profile at $x/D = 1.06$, whereas Parnaudeau et al. obtained a U–shaped profile in their experiments. Then $\langle L_r \rangle / D$ is 1.51 in Parnaudeau et al. , while Lourenco and Shih obtained 1.18. The evident differences in the shape and size of the recirculation region thus relate to the above-cited experimental data.

Concerning the present simulations, as shown in Fig. 8, only the SA–IDDES and $\overline{v^2}$–f DES models predict a U–shaped profile with our finer grid (G1), whereas the NLDES and SA–DES techniques produce a V–shaped profile at $x/D = 1.06$ with both the G1 and the G2 grid. Note too that all the computations presented here are mostly in agreement for $x/D \geq 4.0$ with the experiments conducted by Ong and Wallace, [17].

Kravchenko and Moin, [23], suggested that the shape of the mean velocity profile is strictly linked to an early transition in the shear layers. The streamwise velocity fluctuations, Fig. 10, are indeed noticeably higher for all the employed models when the coarser grid is adopted, for instance. In addition, the instantaneous vorticity magnitude contour plots, shown in Fig. 11 for the $\overline{v^2}$–f model for compactness, demonstrate that the separating shear layers are much longer in the simulations with a finer resolution, Fig. 11(a), than in the coarse grid, Fig. 11(b). In other words, for all the DES models tested,

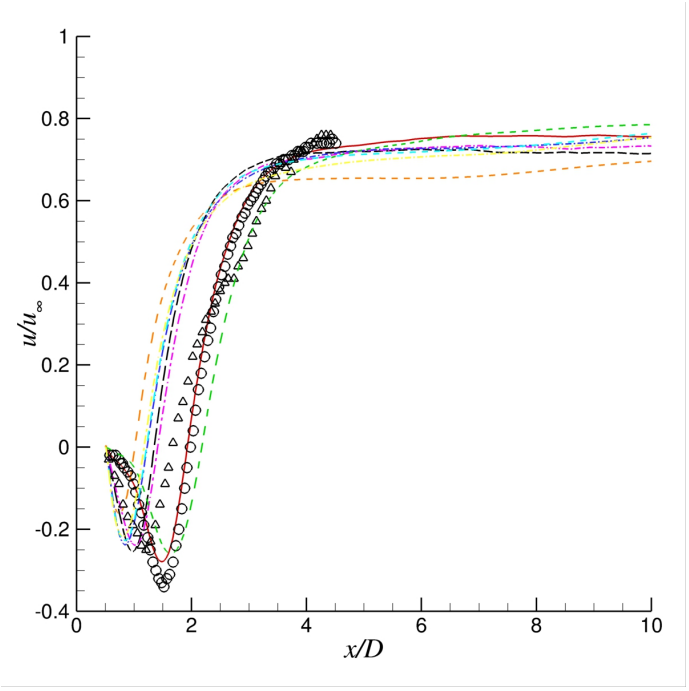

Figure 7. Mean streamwise velocity in the wake centerline, comparing grids G1 and G2.
Legend:- - -SA–DES (G1), - - -SA–DES (G2), -·- NLDES (G1), -·- NLDES (G2), — SA–IDDES (G1), - - - SA–IDDES (G2), - - - $\overline{v^2}$–f DES (G1), -·- $\overline{v^2}$–f DES (G2), ○ Exp. Parnaudeau et al., △ Exp. Lourenco and Shih, □ Exp. Ong.

the coarser grid (G2) is certainly inadequate for solving the thin shear layers developing behind the cylinder, and this leads us to obtain an early transition (shorter shear layers). So there was probably an early transition in the shear layers in the experiments conducted by Lourenco and Shih, as already mentioned by Kravchenko and Moin [23]. This factor should explain the agreement Lourenco and Shih findings and the under–solved computations.

It is also worth mentioning that the standard SA–DES model, and its non–linear version (NLDES), are unable to solve the wake region accurately even with our finest grid (G1). Generally speaking, the coarse–grid computations and the SA–DES/NLDES on the G1 grid show a smaller recirculation region and a weaker velocity deficit by comparison with the finest solutions.

The effect of spanwise resolution was also investigated by carrying out a set of

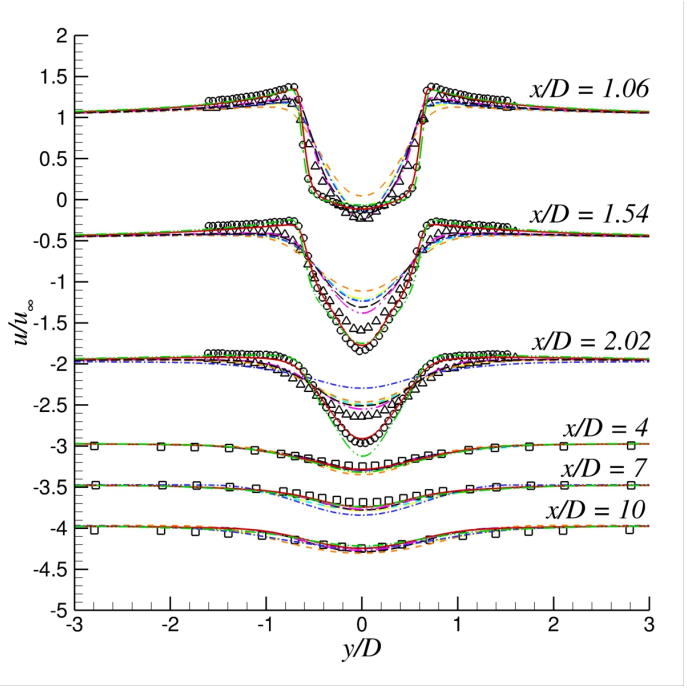

Figure 8. Mean streamwise velocity at different locations in the wake region, comparing grids G1 and G2. For details, see the caption for Fig. 7. The velocity profiles are vertically shifted for the sake of clarity.

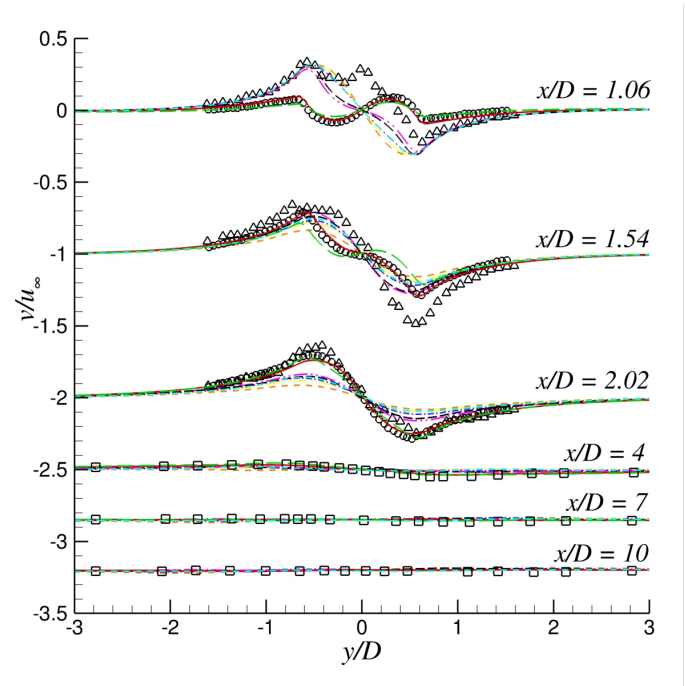

Figure 9. Mean transverse velocity at different locations in the wake region, comparing grids G1 and G2. For details, see the caption for Fig. 7. The velocity profiles are vertically shifted for the sake of clarity.

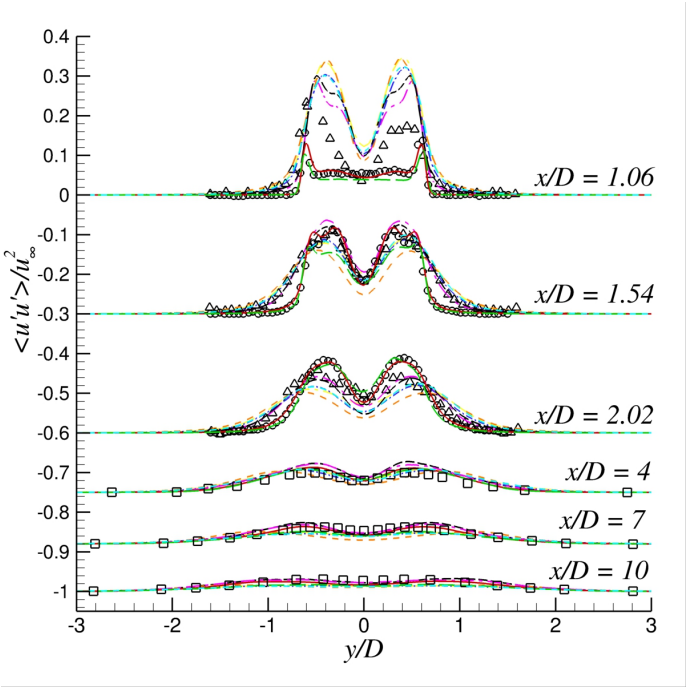

Figure 10. Mean resolved streamwise Reynolds stresses at different locations in the wake region, comparing grids G1 and G2. For details, see the caption for Fig. 7. The velocity profiles are vertically shifted for the sake of clarity.

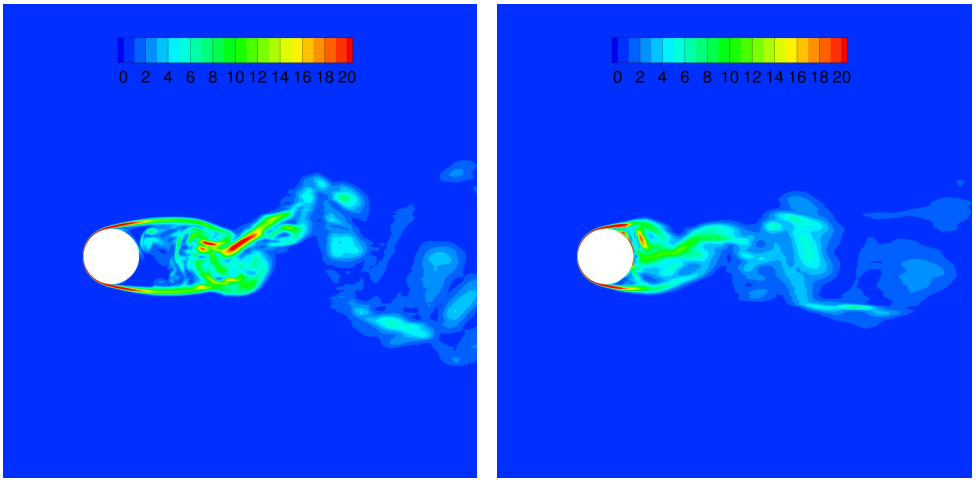

(a) Grid G1 (fine) (b) Grid G2 (coarse)

Figure 11. Instantaneous vorticity magnitude, $\overline{v^2}$–f DES. $T = 500D/u_\infty$.

computations on the G3 grid. The G1 and G3 grids differ only in the number of cells in the z–direction, Table 1. It is very easy to see that, for the DES models considered, having only 8 nodes in the direction of the cylinder axis is not enough to capture the important streamwise vortices, see Figs. 12–15.

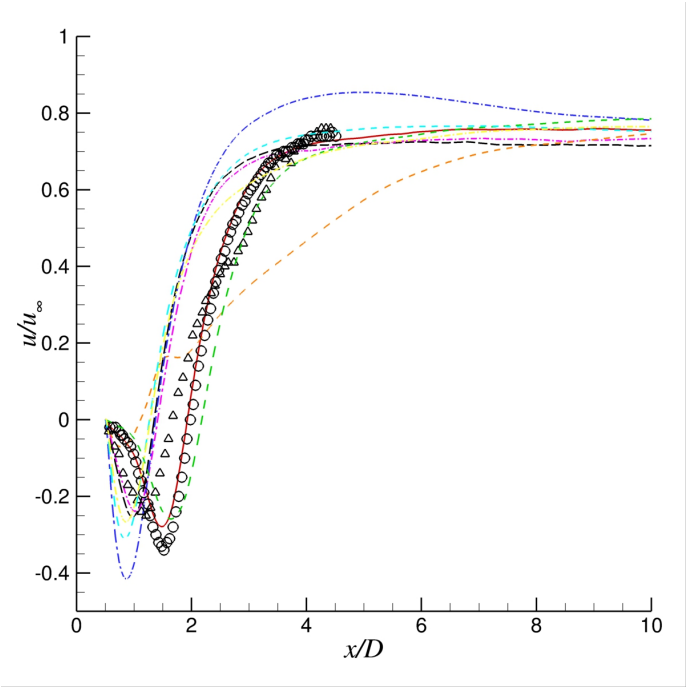

Figure 12. Mean stream–wise velocity in the wake centerline. G1 and G3 grids comparison.
Legend:- - -SA–DES (G1), - - -SA–DES (G3), - · - NLDES (G1), - - - NLDES (G3), — SA–IDDES (G1), - - - SA–IDDES (G3), - - - $\overline{v^2}$–f DES (G1), - · - $\overline{v^2}$–f DES (G3), ○ Exp. Parnaudeau et al., △ Exp. Lourenco and Shih, □ Exp. Ong.

At the same time, the effect of the domain's spanwise length was assessed using the G4 and G5 grids with the NLDES approach. These grids have a spanwise length of 0.5 D and they share the same features on the plane normal to the cylinder's axis (with grids G1 and G3 too). The G4 and G5 grids also have a different spanwise resolution, see Table 1. Figs. 16–19 clearly show that the above-cited grids are not useful for studying the flow past a cylinder at $\mathrm{Re} = 3900$. In particular, the mean velocity field is completely different from the reference data in the very near wake ($x/D \leq 2.02$), while a sufficient degree of accuracy is achieved for $x/D \geq 4$. Here again, the Reynolds stresses, Fig. 19, are systematically overestimated. This effect is obviously related to the domain size $L_z = 0.5D$, which severely restricts the development of the vortical structures.

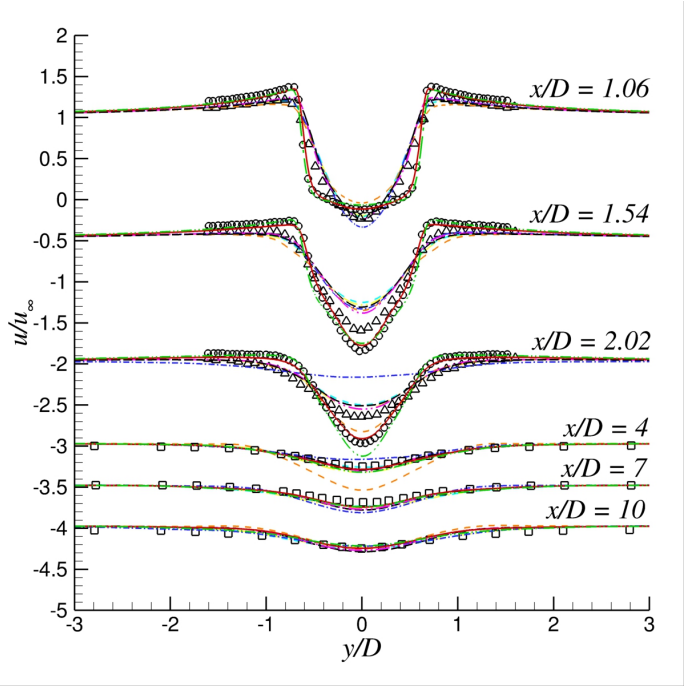

Figure 13. Mean stream–wise velocity at different locations in the wake region. G1 and G3 grids comparison. For details, see the caption for Fig. 12. The velocity profiles are vertically shifted for the sake of clearness.

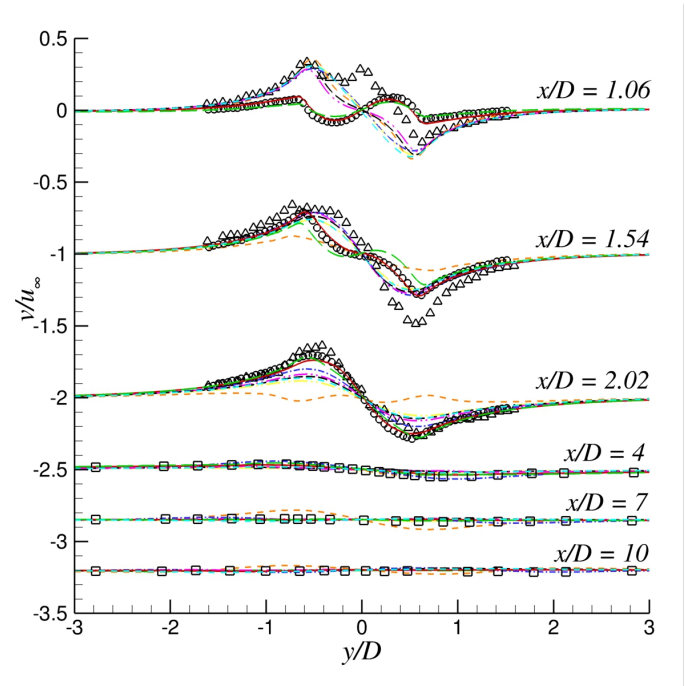

Figure 14. Mean transverse velocity at different locations in the wake region. G1 and G3 grids comparison. For details, see the caption for Fig. 12. The velocity profiles are vertically shifted for the sake of clearness.

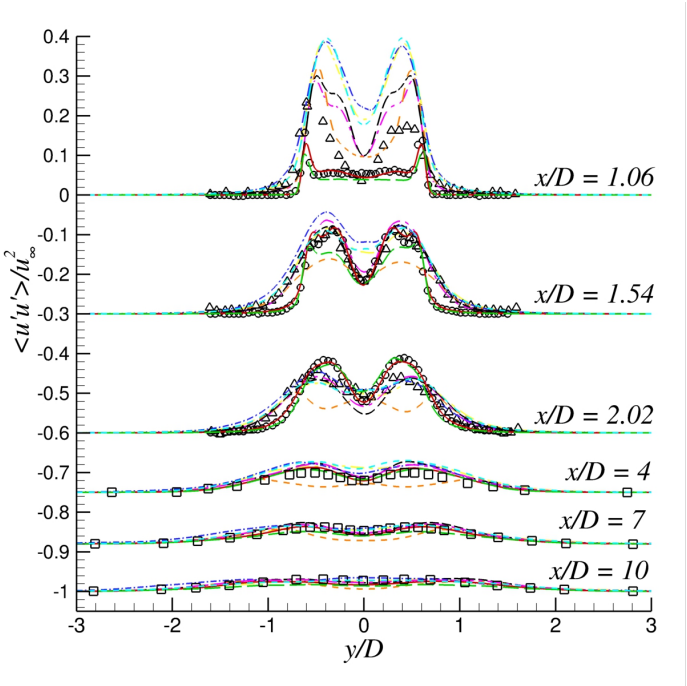

Figure 15. Mean resolved stream–wise Reynolds stresses at different locations in the wake region. G1 and G3 grids comparison. For details, see the caption for Fig. 12. The velocity profiles are vertically shifted for the sake of clearness.

Finally, the effect of the free–stream $\tilde{\nu}$ was investigated to further validate the NLDES approach. In particular, we computed the flow field past the cylinder using the NLDES technique and the condition $\tilde{\nu}_\infty/\nu = 0$ (corresponding to a fully laminar inflow). The flow case considered in this paper regards the sub–critical regime, so the boundary layer is laminar and the laminar–turbulent transition only occurs after the separation. A negligible impact of the free–stream condition for $\tilde{\nu}$ is therefore expected on the flow statistics in the wake region. Figs. 16–19 confirm as much, since it is very obvious that NLDES results obtained with $\tilde{\nu}_\infty/\nu = 3$ and $\tilde{\nu}_\infty/\nu = 0$ are very similar.

4.1.2 Comparison with data in the literature

In this subsection we report flow statistics deriving from our different approaches obtained using the finest grid (G1). A detailed comparison is also

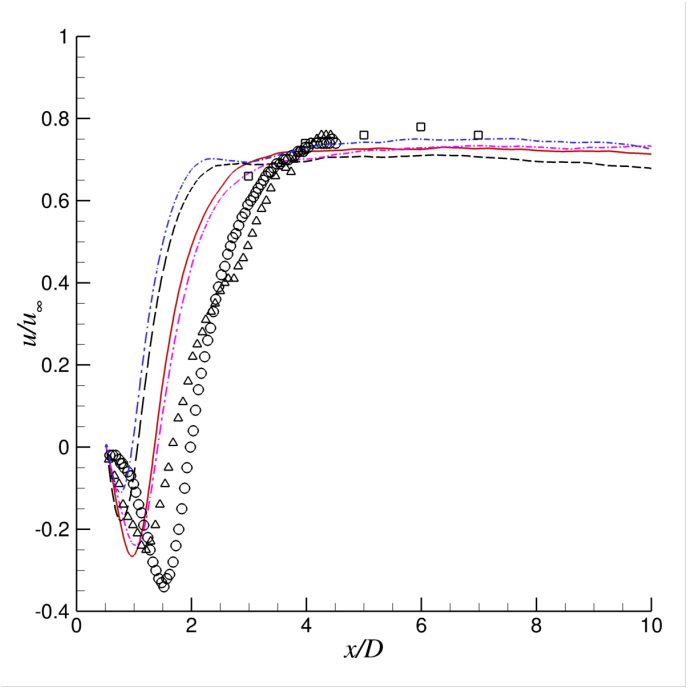

Figure 16. Mean stream–wise velocity in the wake centerline. NLDES model behavior.
Legend: NLDES ($\tilde{\nu}_\infty/\nu = 3$, G1), NLDES ($\tilde{\nu}_\infty/\nu = 0, G1$), NLDES ($\tilde{\nu}_\infty/\nu = 3$, G4), NLDES ($\tilde{\nu}_\infty/\nu = 3$, G5), ○ Exp. Parnaudeau et al., △ Exp. Lourenco and Shih, □ Exp. Ong. The velocity profiles are vertically shifted for the sake of clearness.

drawn with the experimental data in the literature introduced in Sec. 4.1.1 . The present solutions are compared with the CFD computations by Lysenko et al., [26], who performed LES (with Smagorinsky SGS and a turbulent kinetic energy equation) using OpenFOAM compressible solvers.

Fig. 20 shows the mean streamwise velocity along the centerline in the wake region. As already mentioned, this plot can be used effortlessly to estimate $\langle L_r \rangle / D$. This is a crucial matter because the quality of $\langle L_r \rangle / D$ predictions can be considered as the deciding factor for the agreement between experimental and numerical results, [16]. It is worth emphasizing that the present predictions, based on SA–IDDES, closely resemble the reference data. In particular, $\langle L_r \rangle / D$ computed by our SA–IDDES solution is 1.427, while we obtained $\langle L_r \rangle / D = 1.678$ with our $\overline{v^2}$–f implementation. This set of results is

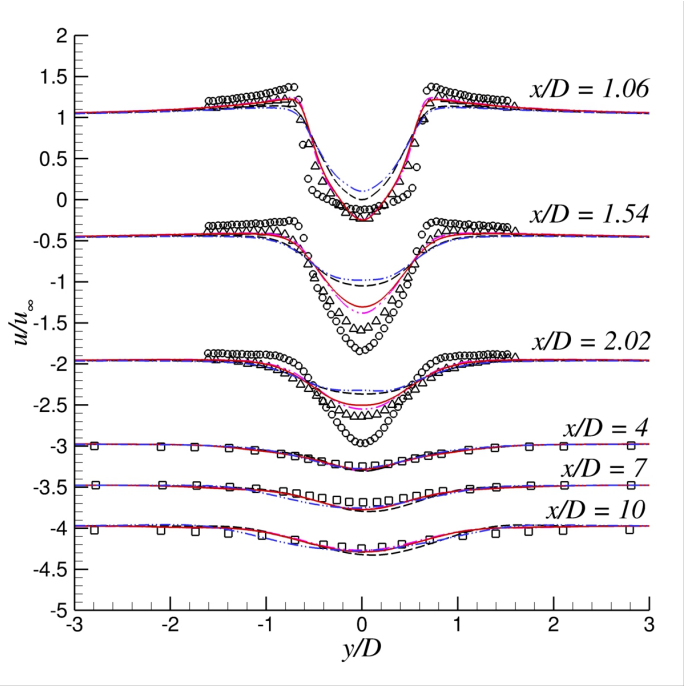

Figure 17. Mean stream–wise velocity at different locations in the wake region. NLDES model behavior. For details, see the caption for Fig. 16. The velocity profiles are vertically shifted for the sake of clearness.

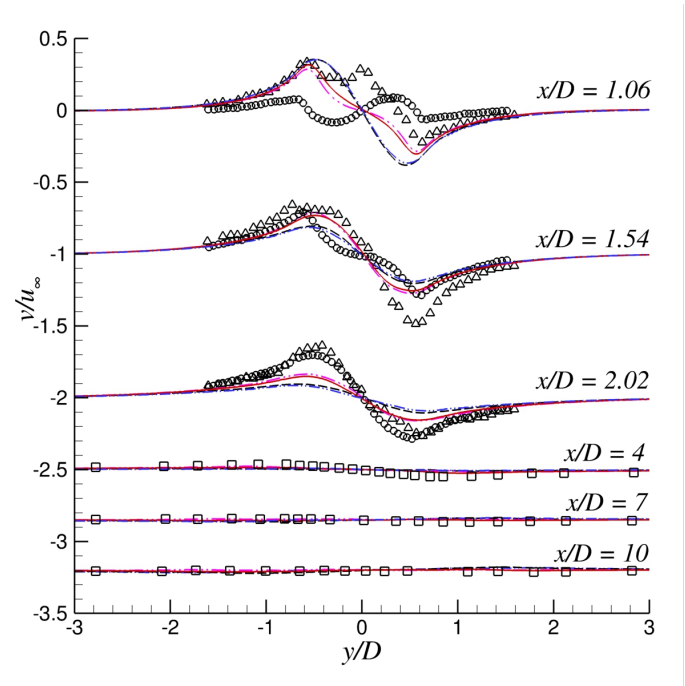

Figure 18. Mean transverse velocity at different locations in the wake region. NLDES model behavior. For details, see the caption for Fig. 16. The velocity profiles are vertically shifted for the sake of clearness.

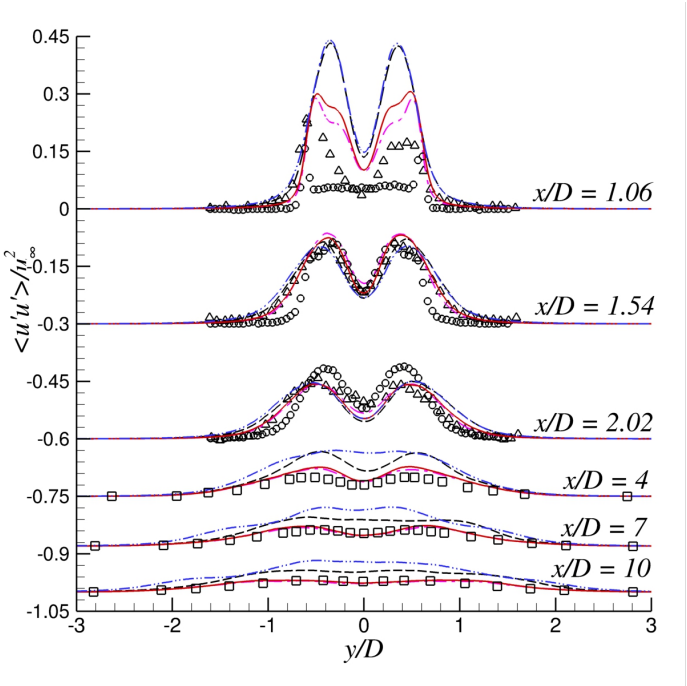

Figure 19. Mean resolved stream–wise Reynolds stresses at different locations in the wake region. NLDES model behavior. For details, see the caption for Fig. 16. The velocity profiles are vertically shifted for the sake of clearness.

consistent with the experimental data in Parnaudeau et al., [16] who predicted $\langle L_r \rangle / D = 1.51$. Lysenko et al., using TKE–LES, [26], and Jee and Sheriff using $\overline{v^2}$-f DES, predicted 1.68 and 1.44, respectively. Our approaches based on standard SA–DES, *i.e.* both the linear and the non–linear techniques, show a good agreement with Smagorinsky LES results, as in Lysenko et al. [26]. In this case, $\langle L_r \rangle / D$ is clearly underestimated, however, compared with the PIV data in Parnaudeau et al., [16]. A complete review of the results in the literature for $\langle L_r \rangle / D$ is given in Table 4.

Fig. 21 shows the mean streamwise velocity profiles in the cylinder's wake. Our SA–IDDES and $\overline{v^2}$–f DES generated a U–shaped velocity profile very consistent with the TKE–LES data in [26], and with Parnaudeau's experimental data, [16]. At the same time, the velocity profiles calculated with NLDES and SA–DES exhibit a V–shaped profile and a very good agreement

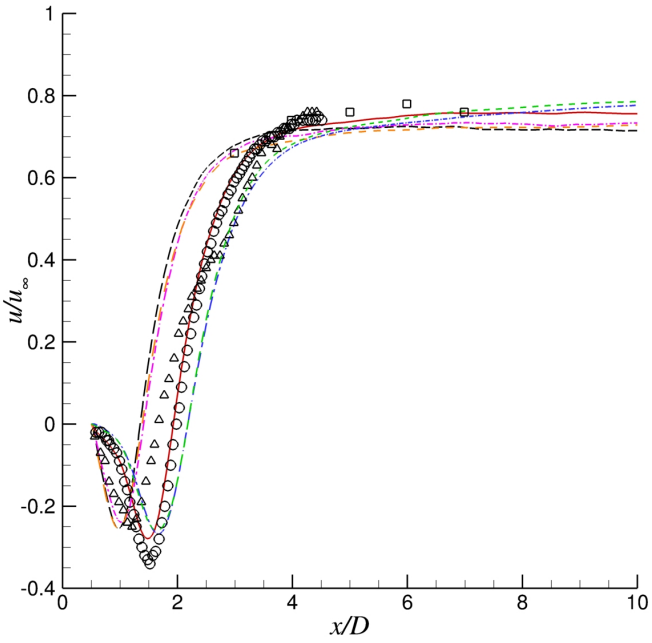

Figure 20. Mean streamwise velocity in the wake centerline. Comparison with data in the literature.
Legend: NLDES, SA–DES, SA–IDDES, LES–TKE ([26]), LES–SMAG ([26]) ,$\overline{v^2}$–f DES, ○ Exp. Parnaudeau et al., △ Exp. Lourenco and Shih, □ Exp. Ong.

with the experimental findings of Lourenco and Shih, [15], and with the OpenFOAM Smagorinsky–LES results in Lysenko et al., [26]. For $x/D = 1.54$ and $x/D = 2.02$, only the SA–IDDES and $\overline{v^2}$–f models are consistent with the findings of Parnaudeau et al., [16], and Lysenko et al., [26], using TKE–LES, whereas the SA-DES and NLDES show a good agreement with the PIV data in Lourenco and Shih, [15], and with the Smagorinsky LES in Lysenko et al., [26]. All of our computations for $x/D \geq 4.0$ are fairly consistent with the experiments conducted by Ong and Wallace, [17], and with the data reported by Lysenko et al., [26].

Fig. 22 shows the mean transverse velocity profiles, v/u_∞. Once again, the present SA–IDDES and $\overline{v^2}$–f results are in line with the experiments conducted by Parnaudeau et al., [16], and with the data reported by Lysenko et al. TKE–LES, [26]. The NLDES and SA–DES compare particularly well with

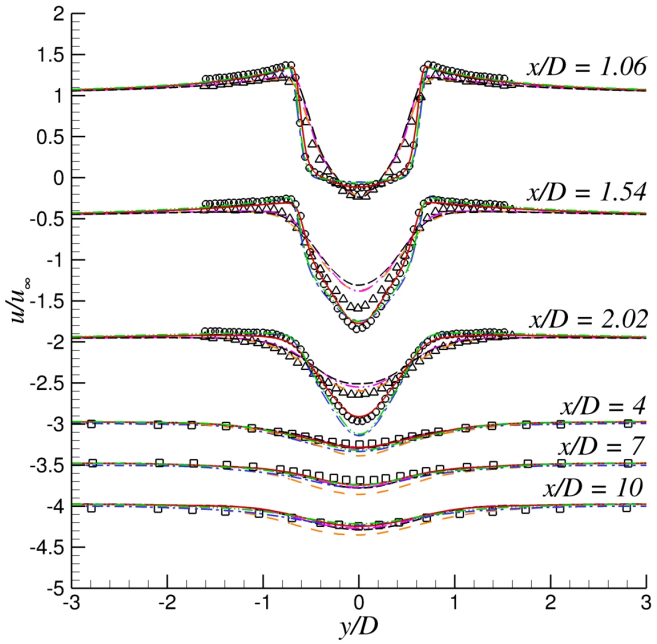

Figure 21. Mean streamwise velocity at different locations in the wake region. Comparison with data in the literature. For details, see the caption for Fig. 20. The velocity profiles are vertically shifted for the sake of clarity.

the experimental data in Lourenco and Shih, [15], and the Smagorinsky SGS based LES findings in Lysenko et al., [26]. For the profiles where $x/D \geq 4$ all the results presented here agree well with each other and with those of Ong and Wallace, [17].

Fig. 23 shows the solved Reynolds normal stress, $\langle u'u' \rangle / u_\infty^2$. Both SA–IDDES and our $\overline{v^2}$–f DES implementation proved capable of capturing these two peaks very well. Fig. 23 also shows that TKE–LES is unable to accurately compute the peaks' magnitude; in a sense, this goes to show the efficacy and reliability of our DES approaches. The standard SA–DES and NLDES techniques agree, here again, with Lourenco and Shih, [15] and the Smagorinsky LES data in Lysenko et al. [26]. Note that, at $x/D = 1.54$, only SA–IDDES is consistent with Parnaudeau et al., [16], whereas $\overline{v^2}$–f and LES–TKE tend to underestimate $\langle u'u' \rangle / u_\infty^2$. Finally, a good agreement emerges between all the present calculations and the data in the literature for $x/D \geq 2.02$.

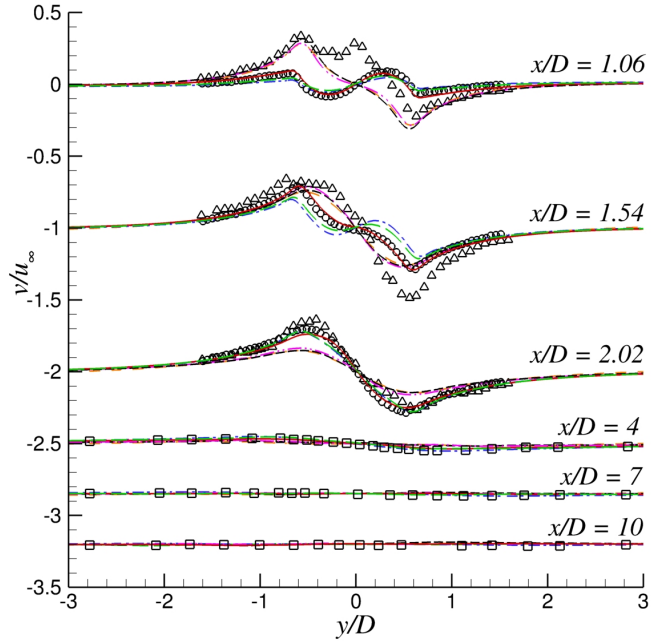

Figure 22. Mean transverse velocity at different locations in the wake region. Comparison with data in the literature. For details, see the caption for Fig. 20. The velocity profiles are vertically shifted for the sake of clarity.

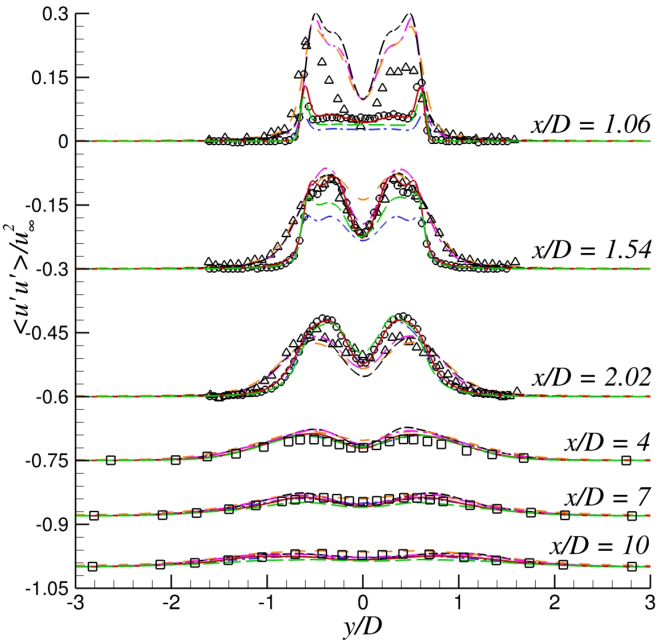

Figure 23. Mean resolved streamwise Reynolds stresses at different locations in the wake region. Comparison with data in the literature. For details, see the caption for Fig. 20. The Reynolds stresses component profiles are vertically shifted for the sake of clarity.

Results concerning the mean cross-flow normal Reynolds stress $\langle v'v' \rangle / u_\infty^2$ are shown in Fig. 24. It is clear that SA–DES and NLDES overestimate the Reynolds stress for $x/D = 1.06$ and $x/D = 1.54$, while for other profiles they are consistent with experimental data sets. On the other hand, the SA–IDDES results are consistent with the reference data in the very near wake as well as in the other positions. The same can be said of the $\overline{v^2}$–f technique, but this model exhibits a $\langle v'v' \rangle / u_\infty^2$ underestimation for $x/D = 1.54$ and $x/D = 2.02$, as seen with the TKE–LES approach, [26].

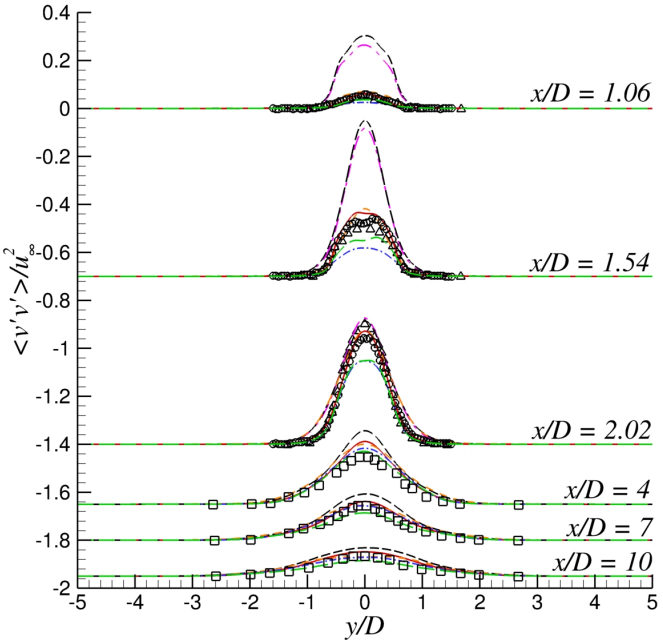

Figure 24. Mean solved transverse Reynolds stresses at different locations in the wake region. Comparison with data in the literature. For details, see the caption for Fig. 20. The Reynolds stresses component profiles are vertically shifted for the sake of clarity.

The last plot shows the solved streamwise Reynolds stress in the wake centerline, see Fig. 25. Experimental data demonstrate that $\langle u'u' \rangle / u_\infty^2$ is zero at the base of the cylinder, and it reaches two peaks before its slow monotonous decay to zero. Some numerical simulations reported here, and in the literature ones [16], do not show the second peak in $\langle u'u' \rangle / u_\infty^2$ profile, but only a

slight step. The $\overline{v^2}$–f DES model seems to exhibit the best agreement with the LES data in Paranadeau et al. and with Norberg's experiments, though the Reynolds stress decay is steeper for our DES results, and the $\langle u'u' \rangle / u_\infty^2$ level in the wake region is lower. SA–IDDES underestimates the $\langle u'u' \rangle / u_\infty^2$ peak, but in the wake region it produces similar results to the $\overline{v^2}$–f approach. Neither SA–DES nor NLDES show the previously-mentioned slight step in their trend, but their peak is comparable with the experimental data, especially using NLDES.

It is also worth noting that the quadratic constitutive relation for the un-

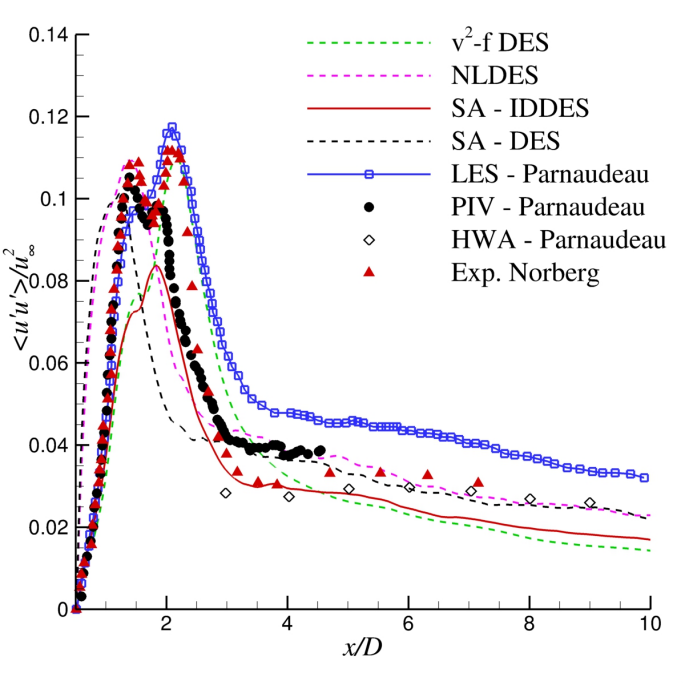

Figure 25. Mean solved streamwise Reynolds stress in the wake centerline. Comparison with data in the literature.

solved terms used in this work, eq. 3, produces some slight effects by comparison with the standard SA–DES model. The most relevant effect is on the $\langle u'u' \rangle / u_\infty^2$ profile at $x/D = 1.06$; in this case, the NLDES approach enables the SA based DES to obtain a very good fit with the Smagorinksy LES in Lysenko et al. [26], see Fig. 21. The NLDES approach also predicts a $\langle L_r \rangle / D$

value closer to the Smagorinsky LES result than standard SA–DES, see Table 4. Taken together, our results confirm that nonlinear constitutive relations in the DES approach might provide a small robust improvement over the basic techniques, as noted by Liu et al., [40], in the LES framework.

4.2 Wall data

In this subsection we present and discuss a series of results related to the cylinder wall. Fig. 26(a) shows the average pressure coefficient distribution, $\langle C_p \rangle = 2\left(\langle p \rangle - p_\infty\right)/\rho u_\infty^2$). Note that, for the sake of brevity, only our results for the G1 grid have been included. It is quite easy to see that the $\overline{v^2}$–f DES results are very similar to the experimental data, [57]; here again, the SA–IDDES data show a slight underestimation of $\langle C_p \rangle$ in the same zone. Other DES approaches proposed here reveal some deviations from the experimental data, as do the Smagorinsky LES findings in Lysenko et al. [26] .

This plot is also very useful for ascertaining the mean base suction coefficient, $\langle C_{p,b} \rangle$, which is $\langle C_p \rangle$ on the cylinder surface at $\theta = 180°$. Table 4 provides a complete review of the integrated flow quantities currently available in the literature. Table 3 shows all the results obtained in the work using the suite of computational grids described in Sec 3.2. Analyzing the above-mentioned tables, it is clear that for $\overline{v^2}$–f we obtained $\langle C_{p,b} \rangle \simeq -0.829$; this with Norberg's, [57], experimental measurements of $\langle C_{p,b} \rangle \simeq -0.84$. SA–IDDES slightly overestimated this value, at $\langle C_{p,b} \rangle \simeq -0.878$, see Table 4. The other DES solutions (on the finest grid) presented here produced $\langle C_{p,b} \rangle$ values close to -1, i.e. they underestimated this value. These results correlate clearly with the nature of the DES approach, in that using the RANS technique in the near-wall region

may give rise to inaccurate wall data a priori. The $\overline{v^2}$–f model performs well for the $\langle C_p \rangle$ distribution too, however, thanks to its ability to predict the near-wall effects accurately.

This situation is reflected in the results for the force coefficients. Fig. 27 shows the time–histories of the instantaneous lift coefficient, C_L, and drag coefficient, C_D, obtained with the SA–DES, SA–IDDES and $\overline{v^2}$–f DES models using the G1 grid. Note that the NLDES results are omitted to simplify the plot contents, given that the presence of the NLDES data is not particularly relevant in this particular case. It is clear that the standard SA–DES overestimates the C_D and C_L coefficients vis-à-vis the SA–IDDES and $\overline{v^2}$–f. In particular, the behavior of the force coefficients relates to the boundary layer detachment mechanism shown in Fig. 28. Standard SA–DES shows an early transition from 2D to 3D flows (very close to the cylinder). SA–IDDES and $\overline{v^2}$–f models are characterized instead by mainly two–dimensional free-shear layers. The features of a laminar flow are consequently retained more in the latter cases than in the standard SA–DES, producing smoothed force coefficient time–histories. In connection with the $C_{L,rms}$ values, see Table 4, we found that a shorter mean recirculation bubble length, $\langle L_r \rangle / D$ corresponds to a higher amplitude of $C_{L,rms}$, as shown in Fig. 20. This situation was first mentioned by Ouvrard et al., [53], and confirmed by Lsyenko et al., [26] for pure LES calculations too. Our SA–IDDES and $\overline{v^2}$–f are generally consistent with several accurate literature references listed in Table 4. Our standard SA–DES and NLDES approaches seem instead to exhibit a better agreement with LES based on the Smagorinsky SGS model.

As concerns the $\langle C_D \rangle$ values, it is easy to see that the results obtained with $\overline{v^2}$–f model on our finest grid produce the best fit with experimental data. The SA–IDDES results are very good too, but they slightly overestimate $\langle C_D \rangle$.

Other approaches proposed here produce a marked overestimation of the average drag coefficient. Fig. 26(b) shows the dimensionless mean vorticity mag-

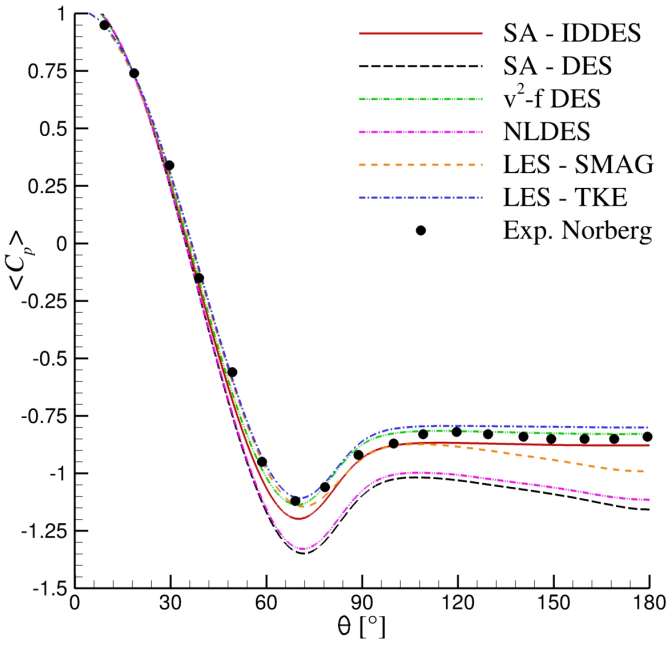

(a) Mean pressure coefficient (grid G1)

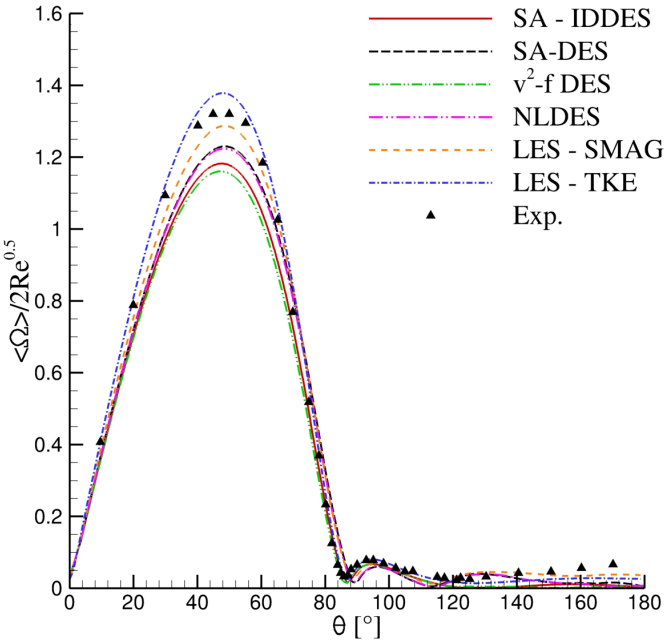

(b) Mean wall vorticity magnitude (grid G1)

Figure 26. Mean wall data.

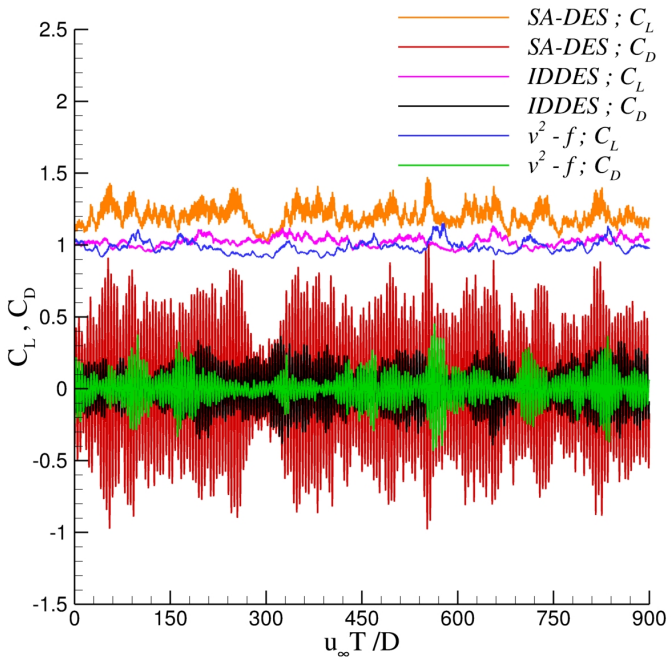

Figure 27. Force coefficient time–histories (grid G1).

nitude, $\langle\Omega\rangle$, on the cylinder surface (here again, only the results for the G1 grid are considered). Note that $\langle\Omega\rangle$ is scaled as in Ma et al., [33], using the factor $2\sqrt{\mathrm{Re}}$. Our DES computations clearly underestimate the wall vorticity magnitude, but a fairly good consistency emerges between our numerical solutions and the reference data in the literature.

A further note concerns the mean separation flow angle, $\langle\theta_{sep}\rangle$. SA–IDDES and our $\overline{v^2}$–f model estimate, using G1 grid, $\langle\theta_{sep}\rangle = 87.0°$ and $\langle\theta_{sep}\rangle = 86.4°$, respectively. These data are within the range of the experimental values and similar to previous DES and LES results, [10, 16, 23, 24, 26, 32]. For this flow quantity, SA–DES and NLDES again overestimate the reference value, Table 4, even though they provide a good fit with the Smagorinsky LES data in Lysenko et al., [26], and other Smagorinsky LES references in the literature. The Strouhal number related to vortex shedding instability was also computed by performing the Discrete Fourier Transform (DFT) of the lift coefficient time signal. For this specific flow parameter all our simulations predict values

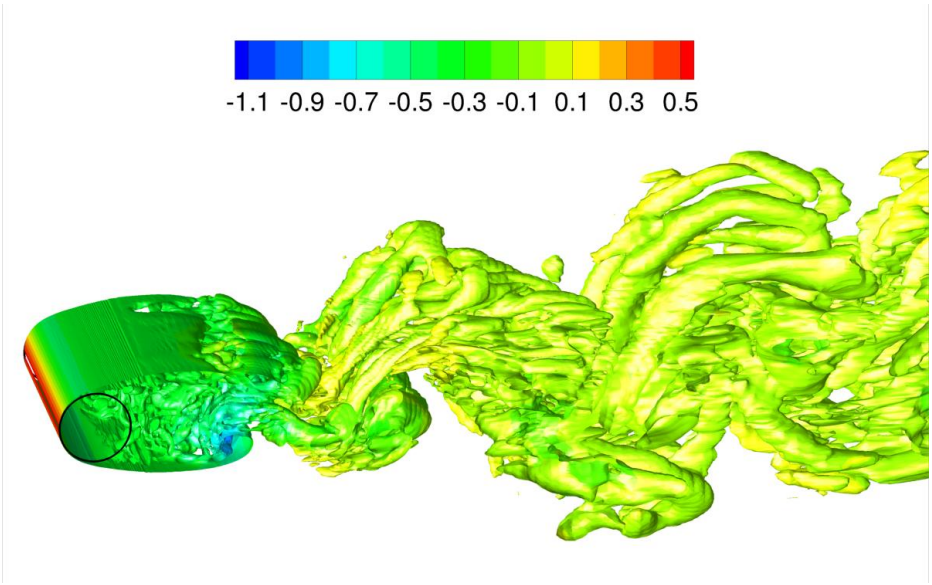

(a) $\overline{v^2}$–f DES

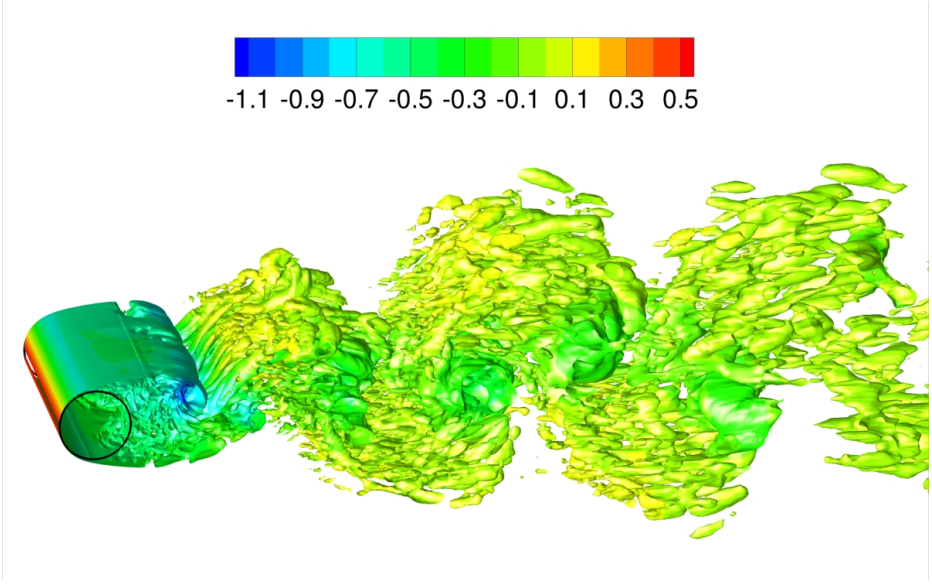

(b) SA–IDDES

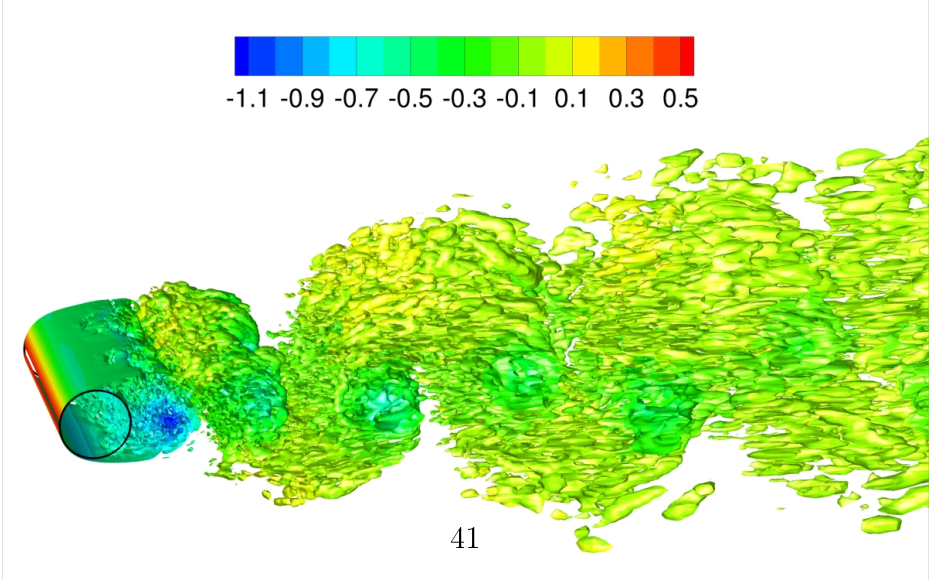

(c) SA–DES

Figure 28. Vortical structure, identified by the Q–criterion, isosurface colored by pressure obtained with the G1 grid. $Q = 0.5u_\infty^2/D^2$ at $T = 500D/u_\infty$.

Table 3
Integrated flow quantities (present solutions). St resolution is $\pm 1.1 \cdot 10^{-3}$ for all the cases.

Grid	Model	$C_{L,rms}$	$\langle C_D \rangle$	St	$-\langle C_{p,b} \rangle$	$\langle L_r/D \rangle$	$\langle \theta_{sep} \rangle$
G1	SA–IDDES	0.1458	1.0235	0.222	0.878	1.427	87.0°
G1	NLDES	0.3832	1.1751	0.217	1.037	0.911	88.99°
G1	SA–DES	0.4248	1.2025	0.215	1.077	0.850	89.28°
G1	$\overline{v^2}$–f DES	0.1088	0.9857	0.214	0.829	1.678	86.40°
G2	SA–IDDES	0.8283	1.4106	0.205	1.4688	0.51375	93.59°
G2	NLDES	0.6546	1.3076	0.207	1.2642	0.6747	91.21°
G2	SA–DES	0.6140	1.2776	0.204	1.289	0.7172	91.08°
G2	$\overline{v^2}$–f DES	0.5719	1.2553	0.205	1.2570	0.7270	90.66°
G3	SA–IDDES	0.5228	1.2501	0.205	1.0376	0.6654	90.02°
G3	NLDES	0.5543	1.2478	0.207	1.1586	0.7842	90.23°
G3	SADES	0.5928	1.2719	0.206	1.1718	0.7694	90.65°
G3	$\overline{v^2}$–f DES	0.5409	1.2452	0.211	0.9726	0.8731	89.80°
G4	NLDES	0.8396	1.4136	0.225	1.5341	0.4661	93.29°
G5	NLDES	0.7273	1.3594	0.222	1.4213	0.5597	92.32°

aligned with the references in the literature, see Table 4. Here too, it is easy to see that all the published data show a very good agreement when predicting the Strouhal number, St.

Integrated flow quantities from coarse grid computations are given in Table 3. All the models were inaccurate in predicting the mean flow parameters on our coarse grids. These computations further confirm that St is not sensitive enough to be a reliable parameter for model validation purposes.

Table 4
Literature integrated flow quantities

	$C_{L,rms}$	$\langle C_D \rangle$	St	$-\langle C_{p,b} \rangle$	$\langle L_r/D \rangle$	$\langle \theta_{sep} \rangle$
Lourenco and Shih PIV, [15]	–	0.99	–	–	1.18	–
Parnaudeau et al. PIV, [16]	–	–	0.21	–	1.51	–
Norberg HWA,[57]	–	0.98	–	0.84	–	–
Lysenko et al. LES–SMAG, [26]	0.444	1.18	0.19	0.8	0.9	89°
Lysenko et al. LES–TKE, [26]	0.09	0.97	0.209	0.91	1.67	88°
Jee $\overline{v^2} - f$ DES, [10]	–	1.0	0.214	0.928	1.44	86.1°
Jee SA-DDES, [10]	–	0.965	0.221	0.969	1.37	88.3°
Parnaudeau et al. LES, [16]	–	–	0.21	–	1.56	–
Mittal et al. LES, [20]	–	1.00	0.22	–	1.588	87°
Kravchenko and Moin LES, [23]	–	1.04	0.21	0.94	1.35	88°
Meyer et al. LES, [24]	–	1.05	0.21	0.92	1.38	88°
Wornom et al. LES, [25]	0.11	0.99	0.21	0.88	1.45	89°
Mani et al. LES, [27]	–	0.99	0.21	0.86	–	89°
Pettersen et al. LES, [29]	0.1954	1.078	0.2154	–	1.27	–
Luo et al. DES, [30]	–	1.01	0.203	0.89	1.46	86.4°
Luo et al. PANS, [30]	–	1.06	0.201	0.96	1.2	87.3°
Zhang et al. LES, [32]	0.125	1.001	0.22	–	–	–
Ouvrard et al. LES, [53]	0.092	0.94	0.22	0.83	1.56	–
Franke et al. LES, [54]	–	0.99	0.21	0.85	1.64	–
Alkishriwi et al. LES, [58]	–	1.05	0.22	–	1.31	–

4.3 Discussion

The flow statistics from the simulations described here, together with the results of other authors' numerical and experimental studies, are reported in the previous sub–sections. A detailed grid study was also conducted, see Sec. 4.1.1. As expected, our results are in line with main references in the literature.

The most important issue emerging vis-à-vis previous plots concerns the different shape of the velocity profiles in the very near wake. Experimental analyses confirmed the existence of two different states for the streamwise velocity, one with a U–shaped profile and the other with a V–shaped profile. In the present work we thoroughly investigated the capabilities of the DES techniques in predicting the flow states behind circular cylinders in the sub–critical regime. Only the SA–IDDES and $\overline{v^2}$–f approaches demonstrated the ability to obtain the U–shaped profile using our finest grid (G1). On the other hand, the standard SA–DES technique has only proved capable of capturing V–shaped velocity profiles. To overcome this limitation, we also introduced a nonlinear term in the constitutive equation for the **B** tensor, but - as in previous attempts described in the literature - we obtained only the limited benefits described in Sec. 4.1.2. The $\overline{v^2}$–f model generated very good results for the complex flow problem considered, even if it was implemented and used in the "standard" DES mode. It is already common knowledge that this model should be able to assure a good prediction performance for several reasons, the first of which is associated with its ability to suppress normal velocity fluctuation at the wall caused by non–local pressure–strain effects, [10]. Several authors have shown that this helps to improve the prediction of separation and reattachment. The SA model, for example, does not distinguish flow anisotropies, and that is why we introduced the non–linear Spalart constitutive relation. For the flow field considered here, this feature of the $\overline{v^2}$–f model is probably not crucially important because we have a laminar boundary layer. Another point to make relating to this issue is the behavior of our models within the attached boundary layer, as introduced at the beginning of this section. It should be noted, however, that eddy viscosity is not exactly zero in the attached boundary layer, but it is small enough for its effects to be negligible, see

Fig. 29. We consequently cannot observe the impact of a given RANS model on the laminar boundary layer computation. It is also worth noting that using a DES approach based on the $\overline{v^2}$–f model should improve the model's prediction capabilities in LES mode. This is correlated with the adoption of a transport equation for SGS kinetic energy that is certainly less empirical than the $\tilde{\nu}$ equation used in SA–DES approaches. This point is certainly suited in the computation of the flow past a cylinder in a sub–critical regime.

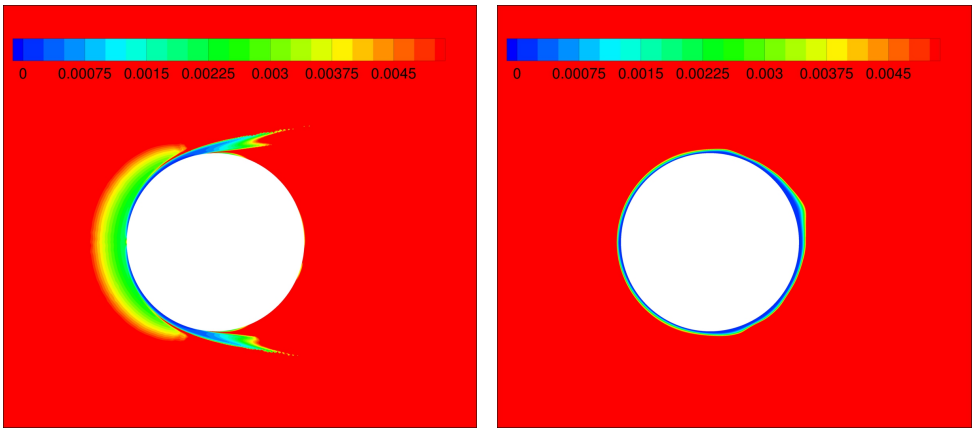

(a) $\overline{v^2}$–f DES (b) SA–IDDES

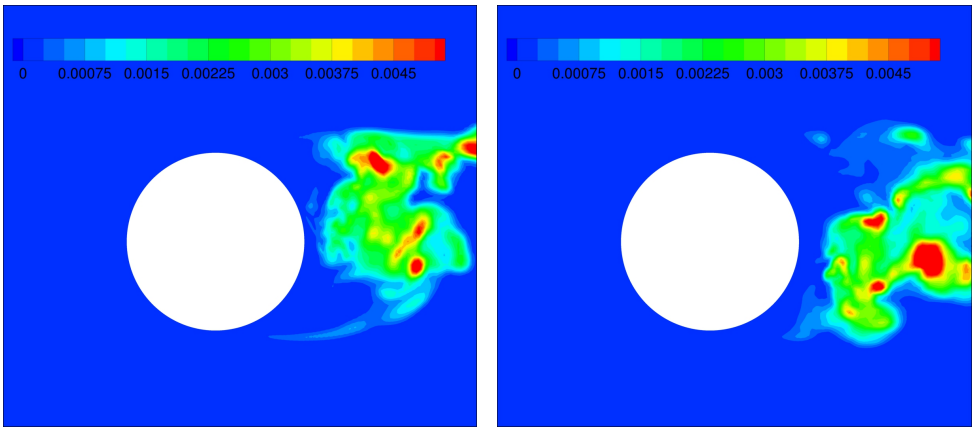

(c) SA–DES (d) NLDES

Figure 29. Contour of a normalized eddy viscosity, ν_T/ν, obtained with the G1 grid. $T = 500D/u_\infty$.

A last comment concerns the SA–IDDES, an approach that - as discussed in Sec. 1 - solves the main problems related to the original SA–DES approaches. A marked improvement in the quality of the results was consequently obtained,

as seen in the previous sub–sections.

In addition, it is very important to emphasize that only the $\overline{v^2}$–f DES model and SA–IDDES (using the G1 grid) are able to solve the separating shear layers accurately. The NLDES/SA–models and the G2 grid proved inadequate for the purpose of solving the shear layers precisely. This is a key issue because we have noted that shear layer under–resolution gives rise to an early transition and strongly influences the recirculation zone and shape.

Another novel feature of this paper worth emphasizing concerns the wall boundary condition used for the ϵ equation in $\overline{v^2}$–f DES. To be more precise, we decided to use a boundary condition developed by Chien [43] for RANS equations rather than the Jee and Shariff proposal, [10]. This enabled us to move the wall boundary condition for ϵ from a Neumann type to a Dirichlet type. From a theoretical point of view, this choice does not affect the quality of the results, while it provides a suitable equivalent boundary condition that is easier to be coded. In conclusion, the $\overline{v^2}$–f model exhibited a good performance requiring greater computational resources were used. For G1 grid the total simulation time for a typical SA–DES/IDDES calculation on GALILEO was about 95 hours (using 384 CPU cores), while the $\overline{v^2}$–f took about 116 hours with the same number of CPU cores. Our $\overline{v^2}$–f results also compare well with those of Jee and Shariff, [10]; the average drag coefficient is very similar to the reference value, and so is the Strouhal number, the $\langle C_{p,b} \rangle$ and $\langle \theta_{sep} \rangle$, see Table 4. The mean recirculation bubble length, $\langle L_r \rangle / D$, estimated from our computations is greater than in Jee and Shariff, [10], but very similar to the figure reported by Lysenko et al., [26], using TKE–LES. Our finest DES results warrant the most attention because a good quality was achieved with a limited number of cells; in fact, these solutions were obtained with coarser

computational grids than those reported in the literature.

Finally, Fig. 30 compares one–dimensional frequency spectra extracted from the present DES solutions in the downstream location at $x/D = 3.0$ on the centerline of the wake. The spectra were obtained on the same interval as was used to compute the flow statistics with the Welch periodogram, [59], a technique based on DFT. A -5/3 slope is shown as well. It is worth noting too that the spectra obtained from our DES computations exhibit similar dissipation features.

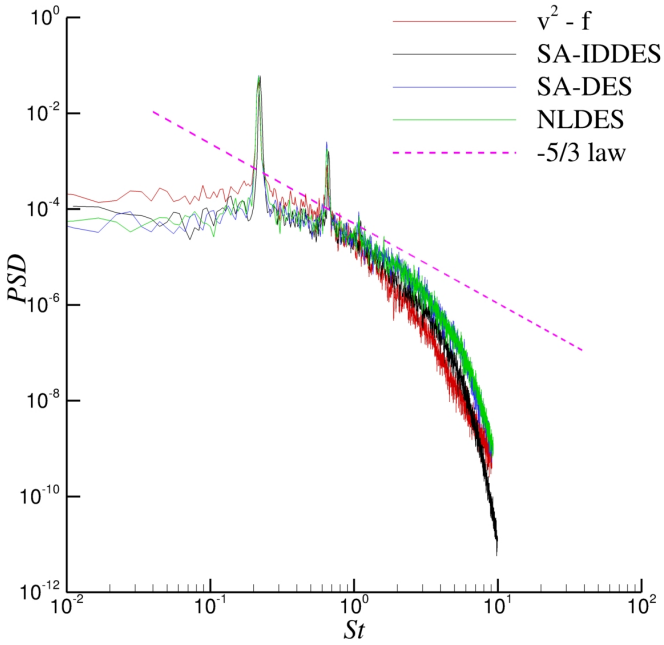

Figure 30. 1–D energy spectrum at $x/D = 3.0$.

5 Conclusions

In this work, we conducted an extensive DES study on the flow past a circular cylinder in the sub–critical regime at Re = 3900. We investigated the DES capabilities of the open–source CFD code OpenFOAM, using standard SA–DES

was used as well as its IDDES modification. We also exploited the open–source features of OpenFOAM to implement two other DES approaches. We considered the very recent $\overline{v^2}$–f DES model equipped with a Dirichlet-type wall boundary condition for ϵ equation; and we implemented a quadratic constitutive relation for the Reynolds stress tensor in the standard SA–DES model (named NLDES). A detailed grid study was also conducted, see Sec. 4.1.1. As expected, the results obtained are consistent with the main references in the literature.

It is worth noting that supercomputing facilities are absolutely necessary in order to run turbulence simulations within an acceptable time frame. That is why we conducted extensive scalability tests in order to make proper use of the GALILEO supercomputing facility at CINECA. The data provided here are clearly of particular interest to OpenFOAM users interested in HPC computing.

We obtained a good feedback with the native OpenFOAM implementation as well as with our own. The significance of our work is not limited to OpenFOAM validation. We also extensively studied the flow considered within the DES framework, and this is of particular interest because the literature contains a great variety of studies for the cylinder at Re = 3900 based on the LES technique, but only a few based on DES computations.

It is also worth emphasizing that (for mean streamwise velocity) the U–shaped profile can only be predicted by SA–IDDES and $\overline{v^2}$–f, whereas - even using our finest grid - standard SA–DES with linear or quadratic constitutive relations can only predict the V–shaped profile in the wake region. The NLDES technique offers some improvement in flow quantity prediction, however, by comparison with the original standard SA–DES model. Our work thus confirms that non–linear constitutive relations for turbulent stresses can slightly

improve the prediction capabilities of the basic techniques, while the $\overline{v^2}$–f DES approach provides reliable and accurate results.

It is also worth noting that our flow statistics are very appealing because they were obtained using less than $4{\cdot}10^6$ grid cells (G1 grid). They are probably the least costly computational results available in the literature (after weighting in terms of quality) because all CFD references use a number of grid cells, n_c, in the range of $5 \cdot 10^6 \leq n_c \leq 10^7$.

We conclude that our results support the adequacy of the OpenFOAM code for computing turbulent flows using DES techniques.

6 Acknowledgements

We acknowledge the CINECA Award N. HP10CV8M72 YEAR 2015 under the ISCRA initiative, for providing high-performance computing resources and support. We are grateful to Dr D. A. Lysenko and Prof. I.S. Ertesvag, Norwegian University of Science and Technology (NTNU), for kindly providing us with their data.

References

[1] P.R. Spalart, W.H. Jou, M. Strelets, and S.R. Allmaras. Comments on the feasibility of LES for wings, and on a hybrid RANS/LES approach. In C. Liu and Z. Liu, editors, *1st AFOSR Int. Conf. on DNS/LES*, Ruston, LA, August 4–8 1997.

[2] P.R. Spalart and S.R. Allmaras. A one-equation turbulent model for aerodynamic flows. *La Recherche Aérospatiale*, 1:5–21, 1994.

[3] P. Spalart. Detached–Eddy Simulation. *Annual Review of Fluid Mechanics*, 41:181–202, 2009.

[4] P.R. Spalart, S. Deck, M.L. Shur, K.D. Squires, M.Kh. Strelets, and A. Travin. A new version of detached-eddy simulation, resistant to ambiguous grid densities. *Theoretical and Computational Fluid Dynamics*, 20(3):181–195, 2006.

[5] M.L. Shur, P.R. Spalart, M.Kh. Strelets, and A.K. Travin. A hybrid RANS-LES approach with delayed-DES and wall-modelled LES capabilities. *International Journal of Heat and Fluid Flow*, 29(6):1638–1649, 2008.

[6] A. Travin, M. Shur, M. Strelets, and P.R Spalart. Physical and numerical upgrades in the detached eddy simulation of complex turbulent flows. In *Proceedings of EUROMECH Colloquium.*, pages 239–254, 2002.

[7] J. Yan, C. Mockett, and F. Thiele. Investigation of alternative length scale substitutions in Detached–Eddy Simulation. *Flow, Turbulence and Combustion*, 74(1):85–102, 2005.

[8] L. Davidson. Evaluation of the SST–SAS model: channel flow, asymmetrical diffuser and axi–symmetric hill. In *European Conference on Computational Fluid Dynamics*, Netherlands, 2006.

[9] F.R. Menter, M. Kuntz, and R. Langtry. Ten years of industrial experience with the SST turbulence model. In *Proceedings of Turbulence Heat and Mass Transfer 4*, 2003.

[10] K. Jee and K. Shariff. Detached–eddy simulation based on the v^2–f model. *International Journal of Heat and Fluid Flow*, 46:84–101, 2014.

[11] M. Mirzaei and A. Sohankar. The evaluation of a detached eddy simulation based on the $k-\omega-v^2-f$ model model with three flow configurations. *Aerospace Science and Technology*, 43:199 – 212, 2015.

[12] N. Ashton, A. West, S. Lardeau, and A. Revell. Assessment of RANS and DES methods for realistic automotive models. *Computers & Fluids*, 128:1 – 15, 2016.

[13] G. Costantinescu and K. Squires. Numerical investigation of flow over a sphere in the subcritical and supercritical regimes. *Physics of Fluids*, 16(5):1449–1465, May 2004.

[14] Xu Change-yue, Chen Li-wei, and LU Xi-yun. Large–eddy and detached–eddy simulations of the sperated flow around a circular cylinder. *Journal of Hydrodynamics*, 19(5):559–563, 2007.

[15] L.M. Lourenco and C Shih. Characteristics of the plane turbulent near wake of a circular cylinder, a particle image velocimetry study, 1993. Published in: Beaudan, P. and Moin, P., Report No. TF62, Thermosciences Division, Department of Mechanical Engineering, Stanford University.

[16] P. Parnaudeau, J. Carlier, D. Heitz, and E. Lamballais. Experimental and numerical studies of the flow over a circular cylinder at Reynolds number 3900. *Physics of Fluids*, 20(8), 2008.

[17] L. Ong and J. Wallace. The velocity field of the turbulent very near wake of a circular cylinder. *Experiments in Fluids*, 20(6):441–453, 1996.

[18] P. Moin. On the order of accuracy of spatial discretization in Turbulent

Flow Simulations. In R. Verzicco, editor, *VORTICAL STRUCTURES AND WALL TURBULENCE*, Rome, September 2014.

[19] P. Beaudan and P. Moin. Numerical experiments on the flow past a circular cylinder at sub-critical Reynolds number, 1994. Report No. TF62, Thermosciences Division, Department of Mechanical Engineering, Stanford University.

[20] R. Mittal and P. Moin. Suitability of upwind-biased finite difference schemes for Large–Eddy simulation of turbulent flows. *AIAA Journal*, 35(8):1415–1417, 1997.

[21] M. Breuer. Large–eddy simulation of the subcritical flow past a circular cylinder: Numerical and modeling aspects. *International Journal for Numerical Methods in Fluids*, 28(9):1281–1302, 1998.

[22] J. Frolich, W. Rodi, Ph. Kessler, S. Parpais, J.P. Bertoglio, and D. Laurence. Large eddy simulation of flow around circular cylinders on structured and unstructured grids. In Hirschel, editor, *Notes in Numerical Fluid Mechanics*, 1998.

[23] A.G. Kravchenko and P. Moin. Numerical studies of flow over a circular cylinder at $Re_D = 3900$. *Physics of Fluids*, 12(2):403–417, 2000.

[24] M. Meyer, S. Hickel, and N.A. Adams. Assessment of implicit large-eddy simulation with a conservative immersed interface method for turbulent cylinder flow. *International Journal of Heat and Fluid Flow*, 31(3):368–377, 2010.

[25] S. Wornom, H. Ouvrard, M.V. Salvetti, B. Koobus, and A. Dervieux. Variational multiscale large–eddy simulations of the flow past a circular cylinder: Reynolds number effects. *Computers and Fluids*, 47(1):44–50, 2011.

[26] D.A. Lysenko, I.S. Ertesvag, and K.E. Rian. Large–Eddy Simulation of

the Flow Over a Circular at Reynolds Number 3900 Using the OpenFOAM toolbox. *Flow, Turbulence and Combustion*, 89(4):491–518, 2012.

[27] A. Mani, P. Moin, and M. Wang. Computational study of optical distortions by separated shear layers and turbulent wakes. *Journal of Fluid Mechanics*, 625:273–298, 2009.

[28] Javad Taghinia and Md Mizanur Rahman and Timo Siikonen. Large eddy simulation of flow past a circular cylinder with a novel sub-grid scale model. *European Journal of Mechanics - B/Fluids*, 52:11 – 18, 2015.

[29] Mia Abrahamsen Prsic and Muk Chen Ong and Bjornar Pettersen and Dag Myrhaug. Large Eddy Simulations of flow around a smooth circular cylinder in a uniform current in the subcritical flow regime. *Ocean Engineering*, 77:61 – 73, 2014.

[30] Dahai Luo, Chao Yan, Hongkang Liu, and Rui Zhao. Comparative assessment of PANS and DES for simulation of flow past a circular cylinder. *Journal of Wind Engineering and Industrial Aerodynamics*, 134:65 – 77, 2014.

[31] Sunghan Kim, Philip A. Wilson, and Zhi-Min Chen. Effect of turbulence modelling on 3-D LES of transitional flow behind a circular cylinder. *Ocean Engineering*, 100:19 – 25, 2015.

[32] Hui ZHANG, Jian min YANG, Long fei XIAO, and Hai ning LU. Large-eddy simulation of the flow past both finite and infinite circular cylinders at Re = 3900. *Journal of Hydrodynamics, Ser. B*, 27(2):195 – 203, 2015.

[33] X. Ma, G.-S. Karamanos, and G.E. Karniadakis. Dynamics and low-dimensionality of a turbulent near wake. *Journal of Fluid Mechanics*, 410:29–65, 2000. cited By 152.

[34] J.G. Wissink and W. Rodi. Numerical study of the near wake of a circular cylinder. *International Journal of Heat and Fluid Flow*, 29(4):1060–1070,

2008. cited By 37.

[35] R. Zhao and C. Yan. Detailed investigation of detached–eddy simulation for the flow past a circular cylinder at Re = 3900. *Applied Mechanics and Materials*, 232:471–476, 2012.

[36] Z.H. Li, J.F. Zhang, and W.Q. Tao. DES turbulence model simulation for flow around circular cylinder at Re = 3900. *Kung Cheng Je Wu Li Hsueh Pao/Journal of Engineering Thermophysics*, 34(9):1703–1706, 2013.

[37] H.G. Weller, G. Tabor, H. Jasak, and C. Fureby. A tensorial approach to computational continuum mechanics using object–oriented techniques. *Comput. Phys.*, 12(6):620–631, 1998.

[38] P.R Spalart. Strategies for turbulence modelling and simulations. *International Journal of Heat and Fluid Flow*, 21(3):252 – 263, 2000.

[39] D.C. Wilcox and M.W. Rubesin. Proposal in Turbulence Modelling for Complex Flow–Fields, 1980. NASA Technical Paper-1517.

[40] Y. Liu, P.G. Tucker, and R.M. Kerr. Linear and nonlinear model large-eddy simulations of a plane jet. *Computers & Fluids*, 37(4):439 – 449, 2008.

[41] H. Gopalan and R. Jaiman. Numerical study of the flow interference between tandem cylinders employing non–linear hybrid URANS–LES methods. *Journal of Wind Engineering and Industrial Aerodynamics*, 142:111 – 129, 2015.

[42] F.S. Lien, G. Kalitzin, and P.A Durbin. RANS modeling for compressible and transitional flows. Proceedings of the summer program, Center for Turbulence Research, 1998.

[43] K. Chien. Predictions of channel and boundary layer flows with a low–reynolds–number turbulence model. *AIAA Journal*, 20:33–38, 1982.

[44] R.I. Issa. Solution of the implicitly discretised fluid flow equations by

operator-splitting. *Journal of Computational Physics*, 62(1):40–65, 1986.

[45] J.H. Ferziger and M. Peric. *Computational Methods for Fluid Dynamics.* Springer, 1999.

[46] B. Geurts. *Elements of Direct and Large-Eddy Simulation.* R.T. Edwards, 2004.

[47] K. Sweby. High resolution schemes using flux–limiters for hyperbolic conservation laws. *SIAM J. Numer. Anal.*, 21:995–1011, 1984.

[48] H. Jasak, H.G. Weller, and A.D. Gosman. High resolution NVD differencing scheme for arbitrarily unstructured meshes. *International Journal for Numerical Methods in Fluids*, 31(2):431–449, 1999.

[49] www.prace-ri.eu. Partenership for Advanced Computing in Europe.

[50] M. Culpo. Current Bottlenecks in the Scalability of OpenFOAM on Massively Parallel Clusters, 2011. PRACE white paper, available on www.prace-ri.eu.

[51] H. Jasak. HPC deployment of OpenFOAM in an industrial setting, 2011. PRACE Seminar: Industrial Usage of HPC.

[52] T. Behrens. OpenFOAM's basic solvers for linear systems of equations, 2009. Technical Report, Chalmers University of Technology.

[53] H. Ouvrard, B. Koobus, A. Dervieux, and M.V. Salvetti. Classical and variational multiscale LES of the flow around a circular cylinder on unstructured grids. *Computers and Fluids*, 39(7):1083 – 1094, 2010.

[54] J. Franke and W. Frank. Large eddy simulation of the flow past a circular cylinder at $\mathrm{Re_D} = 3900$. *Journal of Wind Engineering and Industrial Aerodynamics*, 90(10):1191–1206, 2002.

[55] P.A. Durbin and B.A. Petterson Reif. *Statistical Theory and Modeling for Turbulent Flows,* 2^{nd} *Edition.* Wiley, 2010.

[56] Xia, M. and Karniadakis, G.E. The spectrum of turbulent near wake: A

comparison of DNS and LES. In C. Lui and Z. Lui, editors, *Proceedings of the first ASFOR International conference on DNS/LES*, pages 129–136, 1997.

[57] C. Norberg. An experimental investigation of flow around a circular cylinder: influence of aspect ratio. *Journal of Fluid Mechanics*, 258(0):287–316, 1994.

[58] N. Alkishriwi, M. Meinke, and W. Schroder. A large–eddy simulation method for low Mach number flows using preconditioning and multigrid. *Computers and Fluids*, 35(10):1126–1136, 2006.

[59] P. Welch. The use of Fast–Fourier Transform for the estimation of power spectra: a method based on time averaging over short, modified periodograms. *IEEE Trans. Audio Electroacoust.*, 15(6):70–73, 1967.